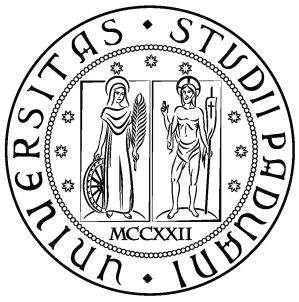

UNIVERSITÀ DEGLI STUDI DI PADOVA

Dipartimento di Fisica e Astronomia "Galileo Galilei"

Corso di Laurea Magistrale in Fisica

Optofluidic application of a Mach-Zehnder interferometer integrated in lithium niobate for droplet sensing

Laureando

Riccardo Zamboni

Relatore

Prof.ssa **Cinzia Sada**

Correlatore

Dr. **Giacomo Bettella**

A.A. 2015-2016

Abstract

In last decades microfluidics has gained an increasing interest by the scientific community due to its capability of control liquids on the microscale. Especially droplet microfluidics technology provides a high manipulation level on very small volumes of fluids. This feature makes it a promising candidate for biological, medical and chemistry applications. With a compact and simple microfluidic device, droplets can be coalesced, mixed, sorted and employed either as micro chemical reactors or as carriers of biological sample.

Most of these applications require a high precision on droplets parameters control such as volume and speed. In many cases these quantities are controlled by external devices like syringe pumps or optical microscopy. Such apparatus cannot provide the function of a single droplet sensor; in case of syringe pumps, they cannot analyse single droplet one by one, and in case of optical microscopy, they cannot measure volume in real time. Thus, sensor of speed and volume for single droplet that are fully integrated on the same substrate will represent an important step for Lab-on-a-chip application. The aim of this thesis' work is to realize and characterize an integrated detector for the measurements of speed and volume of droplets. The measure is simultaneously made on a flux of droplets moving in microchannel, detecting single droplet one by one. The device consists in a novel configuration chip made of lithium niobate, on which a microfluidic circuit and an optical waveguide Mach-Zehnder interferometer (MZI) are integrated on the same platform.

The system is composed of two main stages: Optical and Microfluidic one. The first is a waveguide that divides in two y-branches and two parallel arms to configure MZI. The arms of interferometer are crossed orthogonally by a microfluidic channel, in which droplets are generated by Microfluidic Stage. This one consists in a cross junction, where droplets are

produced by cross-flow of immiscible phases. During the flowing of droplets in the channel, arms of MZI illuminate alternately dispersed and continuous phases. In this way, an intensity signal is collected at the end of MZI, where all information of the droplets can be read thanks to the difference in diffraction index between two liquids.
This novel configuration has several advantages. It can allow for different functionalities such as:

- Measure of droplet speed: it can be detected the time of passing droplet in front of guide.
- Measure of droplet length: it can be easily provided from the time of the flowing of single menisci, both ahead and back.
- Measure of droplet refraction index: with interferometric signal of the different liquids in front of arms.

In this work the geometry of the two main stages are deep investigated in order to optimize the performance of this device. Both cross-junction and MZI in waveguide were already studied in literature, but a low-loss MZI design for optofluidic droplet application has not been mentioned yet. In this work all elements of MZI in waveguide are accurately described with care for low-loss and compatibility with droplet size: from Y-branches to tapered section. Both theoretical and fabrication process studies have been realized on all of key section of MZI configuration. All of them were fabricated in single mode channel waveguide at a wavelength of 632.8 nm by titanium in-diffusion. Subsequently a wide analysis was made in order to guarantee reproducibility: they were optically characterized with Near Field technique. Results were reported and reached performance are highlighted.
After the best configuration was obtained, it has been started studying the optical signal of the flowing droplets. To reach this goal, single waveguide has been used as optical stage, properly coupled with microfluidic one. These samples have helped to understand optofluidics interaction between droplet and guided beam. Promising results have been achieved in this configuration and presented in thesis. First results and tests are reported in this work for MZI configuration with air droplet, four working regimes are founded and studied. The device has been tested with random sequence of droplets in the same running section and MZI signal demonstrated that it can recognize all these droplet in length and velocities reconstructing the sequence.

Contents

Introduction

Optofluidic is newborn research field, where scientists try to integrate Microfluidic and Optic technology in the same device. Interest in this new field come from the wide application, which Microfluidics devices can provide, and on the other hand from the need of these application of integration. Indeed microfludic chips can manipulate and control small amounts of fluids in micrometrics spaces, but most of the cases the system require also bulky instrument like microscope or pumps. This lacks of integration of the detector encourage researchers to include in chips other stages, in order to realize miniaturized, portable Lab-On-a-Chip(LOC). The features of these devices are that they have to perform fast analysis restricted to traditional facilities in small amounts of space.

One of the tools used for this aim is adding a Optical stage to the microfluidic chip. In fact studies about optics integration have been already edited even from seventies for telecommunication applications. Through fibre-optics light can be guided in restricted channels, in the same way done waveguides can be realized on the substrate. First attempts of integration of waveguides in order to interact with microfluidic stage are proposed in [1, 2] simply embedding fiber to the same polymeric matrix for microfluidic stage. Polymeric material have been demonstrated fitting optimally with microfluidics needs, but cannot provide good environment for optical stage. Unlike typical optical material they cannot guarantee stability in time (most of them degrade itself with the time and uses) optically cleanliness and stiffness as vitreous ones.

For these reasons another approach has been taken, which consists in the change of the chip substrate material from polymeric to a more suitable material for integrated optics such as glass or lithium niobate. Better results than polymeric substrate are obtained in [3, 4, 5] on

glass, where waveguides are realized through laser ablation with femtosecond laser source. Optical materials ensure stiffness and chemical inert to the device, which are fundamentals features for development of Chips with high duration and multiple integration stages. This thesis intend to combine both optical and microfluidic stage as single building block for a future integration in a more complex chip. The work aim to contribute to this project with the realization of an prototype for the estimation of volume and velocity of particle, which can be microfluidic droplet or biology sample. The possibility of the detection is a key technology for biochemical application, a technology like this can permit the selection of homogeneous sample from a heterogeneous population. In this work droplet have been studied because they can act as a microreactor for chemical application or as a vector for biologiacl sample, representing a controlled environment.

In this topic, different solution have been proposed, here another new solution is presented: a Mach-Zehnder Interferometer. Interferometer is one of the most used analysis technique due to its sensibility. Specially Mach-Zehnder interferometer with the possibility of having two arms with optical paths completely distincted and once travelled, represents perfect configuration for wide range of application. Different employment have been already developed in Optofluidic for sensing of index of refraction of fluid flowing in microchannels [6, 7] or as a biosensor [8, 9, 10] where biology sample are attached to one arm of the interferometer.

In this thesis a new optofluidic application is presented for Mach-Zehnder interferometer configuration: this is the first time that Mach-Zehnder interferometer is used for droplets sensing. This application aim to resolve the problem of the lack of integration of Microfluidics, caused by the needs of Microscope analysis, thanks to the high level of integration which the chip here presented. In this way lithium niobate as single substrate represents perfect candidate, due to his multiple properties and his famous application in integrated optics. Nevertheless only few works are presented in literature. This material are one possible solution for the realization of a Lab-on-a-Chip completely integrated, portable and independent. In this thesis one step in this direction is done through the realization of a reproducible and calibrated device which simplify typical procedure of measurements.

In particular first Mach-Zehnder interferometer integrated in $LiNbO_3$ for droplet sensing was realized and tested. On the contrary of references cited before, both arms of interferometer are crossed orthogonally by microchannels, where flows droplet. Definitive scheme of the prototype of the Optofluidic device is reported in figure 1. The Lab-on-Chip device of this thesis is designed for both generation and detection of droplets and is completely integrated in the same substrate of Lithium Niobate. The chip is composed of two main stages, which are

properly labelled in the figure 1: first one is a microfluidic droplet generator in cross-junction configuration, while other is a waveguided Mach-Zehnder interferometer. The operating behaviour is the following: through an appropriate light Mach-Zehnder is excited, then interacting with flowing droplet, the optical signal of this interaction is then recollected on the other side with same input waveguide circuit. With the signal length, velocity and index of refraction of droplets can be measured simultaneously with the flows of them and without any additional information about microfluidics condition. This system do not need any Microscope to analyse what happen in the channels. These feature makes the device interesting and innovative for technology of LOCs.

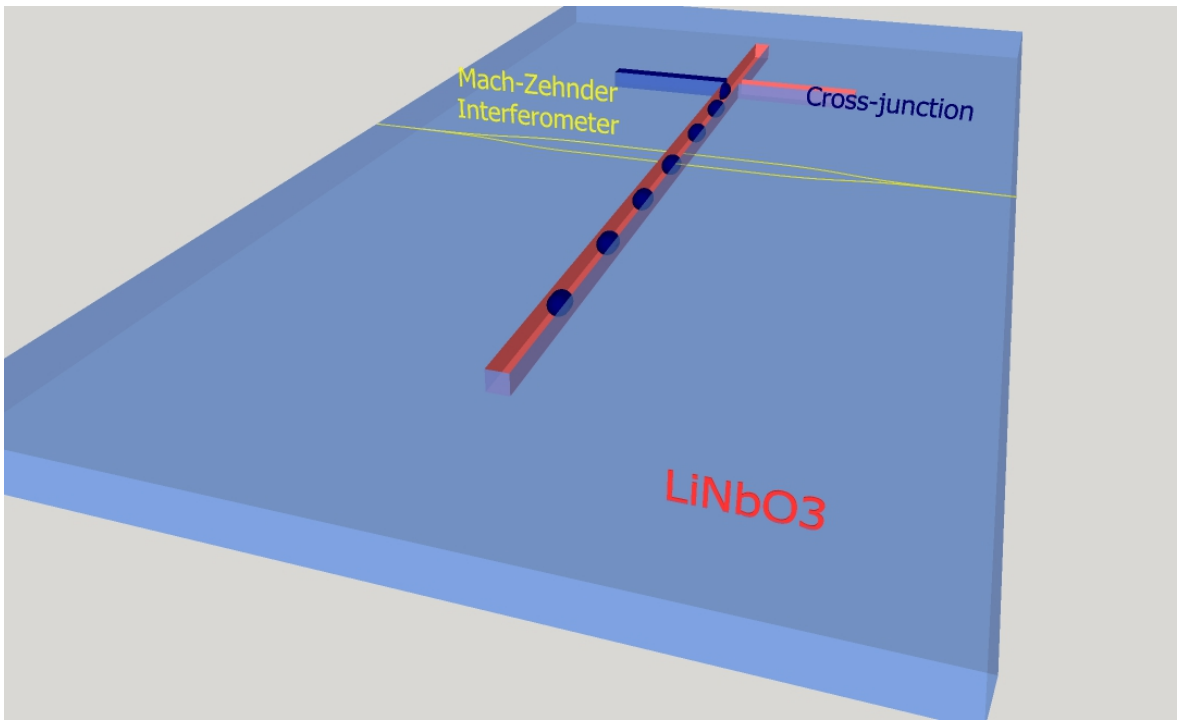

Figure 1: *Sketch of the final aspects of the Optofluidic device of this work. It is composed with two stages: Cross-junction is a droplet producer and an integrated Mach-Zehnder interferometer. The complete device is closed with glass slide and proper inlets for microfluidics liquids*

In this thesis the device has not only presented and characterized, but also all fabrication process: from the design of a low loss integrated Mach-Zehnder Interferometer to the engraving of the microchannels. The contents are distributed as follows:

- In the **Chapter 1** Lithium Niobate is presented as a new valid alternative for substrate of Optofluidic device. All of its properties is briefly discussed from physical point of view, then both microfluidic and well-known integrated optics characteristics are more

deeply discussed.

- In the **Chapter 2** Mach-Zehnder interferometer of the device is analysed from 360 degrees: first low-loss design for optofluidic application is described lingering on the key section, then fabrication method adopted are reported in detail, with all difficulties and relative solutions.

- In the **Chapter 3** all experimental setups needed for the this work both for measurements and for characterizations are illustrated: from optical apparatus and detector to software used for statistical analysis.

- In the **Chapter 4** finally first results of Mach-zehnder configuration for droplet sensing are presented. Also in this chapter there are some preliminary measurements deriving from different optofluidic device, used to understand the interaction between waveguide and flowing droplets.

CHAPTER 1

Lithium niobate: Optofluidic crystal

First chapter is about a brief review of main properties of lithium niobate. Special care is reserved for optofluidic aspect, which are new point of view for lithium niobate, emerged in the last years. Its biocompatibility and strong resistance to all chemical reactions make him perfect candidate to microfluidic application. These features combined with its multiple optical properties indicate $Linbo_3$ as a optimal candidate for Lab-On-a-Chip. This concept born in last years due to the need of miniaturized devices, which can perform analysis typically restricted to traditional laboratories. For this reason, the challenge of research is to integrate more stages as possible on single substrate. Lithium niobate represents one of the best solution for this aim: optical integration is already studied from the seventies, some interesting results for microfluidic circuit has been found in last years from droplet generator [11] to control via electrophoresis [12, 13, 14], and its multiple and different properties do not put in searching limit for new integrations. An outlook of these properties is reported in first section 1.1. Then in section 1.2. Microfluidics in lithium niobate is presented, with special care of the microfluidic circuit used for this work and its fabrication. While in section 1.3 integrated optics in $LiNbO_3$ is reviewed, specially waveguide in lithium niobate and fabrication process are highlighted.

1.1 Lithium Niobate Crystal and Main Properties

1.1.1 Compositional and crystallographic properties

Lithium niobate is a synthetic material, which appears solid, transparent and not soluble in water or organic solvents. It belongs to pseudo-binary system Li_2O-Nb_2O_5 with $Li_2Nb_{28}O_{71}$, Li_3NbO_4 and lithium triniobate $LiNb_3O_8$. The most popular way to product it is via bulk growth by the Czochralsky technique. The molar fraction of Li_2O and of Nb_2O_5 at grown is usually *congruent* composition, which corresponds to 48.6 mol% for Li_2O and near to 51.4 mol% for Nb_2O_5. This composition is at the maximum in the liquid-solid curve, as shown in the phase diagram in figure 1.1. In others case, composition of the crystal varying during the growth, compromising crystal properties and uniformity. In fact phase transition temperature, photovoltaic effect, birefrangence and UV band absorption edge strongly depend on the ratio between the concentration of lithium and niobium [15] Indeed congruent composition is preferred in most of the cases because $LiNbO_3$ growth is reproducible and controlled. In this work Lithium Niobate is bought by Crystal Technology, which sell wafer with 48.38% $\pm$ 0.01 mol% of Li_2O and 51.62% $\pm$ 0.01 mol% of Nb_2O_5.

Lithium niobate is a crystal, which exhibits a mirror symmetry about three planes that are

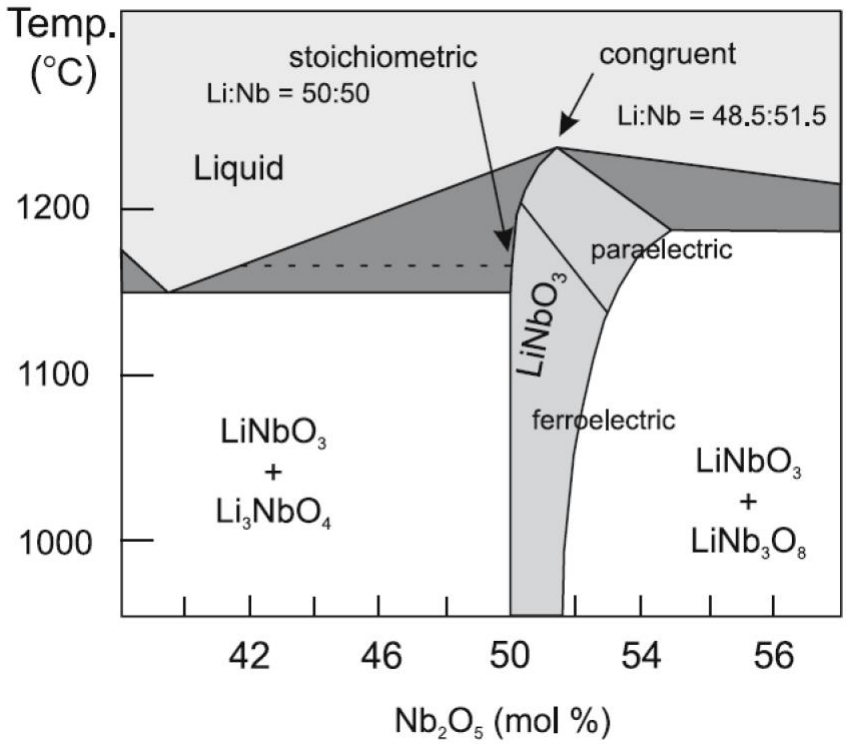

Figure 1.1: *Phase diagram of the Li_2-Nb_2O_5 system [16]*

60°apart. Three-fold rotational symmetry around the axis in intersection of this three planes.

These symmetries classify $LiNbO_3$ in the space group R3*c*, with point group 3*m*. There are 3 possible choices as frame reference: hexagonal, rhombohedral and orthohexagonal. In literature authors usually refer to the orthohexagonal one, which are reported in figure 1.2. This cell is described by the following axes: *z* along the axis of three-fold rotation symmetry,

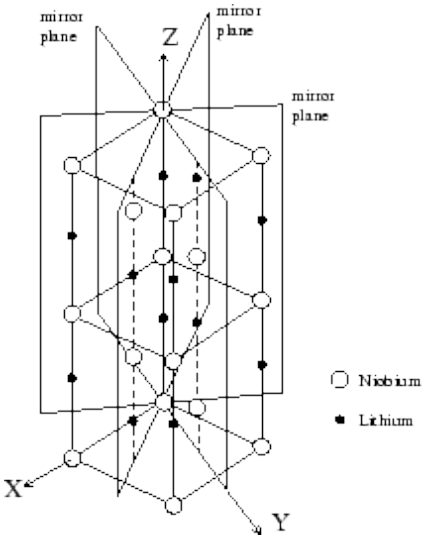

Figure 1.2: *orthohexagonal cell of $LiNbO_3$*

y laying on mirror plane and *x* perpendicular to others. Directions of these axes are decided by convention using piezoelectricity: z axis points on the negatively charged plane under uniaxial compression.

Atomic structure of lithium niobate depends on ferroelectric or paraelectric phase of the crystal. The structure consists of planes of oxygen in a slightly distorted hexagonal close-packed configuration (see 1.3). Octahedrals formed by this oxygens, are regularly filled by lithium atoms, niobium and vacancy, following this order along c axis. Below Curie temperature ($T_C \sim 1160$°Cin ferroelectric phase) lithium atoms are shifted by 44pm from plane of oxygens and niobium atoms by 27pm from the center of octahedra. The spontaneous polarization of ferroelectric phase is caused by these shifts. While in paraelectric phase both shifts of lithium and niobium are zero.

1.1.2 Defect and doping

Impurities and dopants are extremely important in lithium niobate, since structure and properties can be modified. Structure modifications are also important because congruent structure (see previous section) has a lack of about 6% of lithium atoms respect to the stoichiometric one. Thus some sort of structure modification is needed to guarantee charge

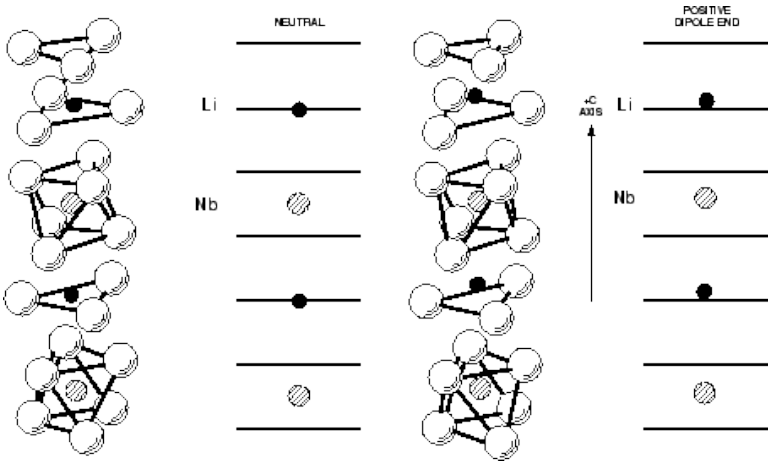

Figure 1.3: *atomic structure of $LiNbO_3$ in ferroelectric phase (right) and paraelectric (left)*

compensation after Li_2O out-diffusion. There are some models about this theme:

- **oxygen vacancy model**: lithium oxide out-diffusion is compensated by oxygen vacancies:

$$\langle \mathrm{LiNbO_3} \rangle \longrightarrow 2V_{\mathrm{Li}}^{+} + V_{\mathrm{O}}^{2-} + \mathrm{Li_2O}$$

- **lithium vacancy model**: lithium vacancies are compensated by niobium atoms:

$$\langle \mathrm{LiNbO_3} \rangle \longrightarrow 4V_{\mathrm{Li}}^{-} + Nb_{\mathrm{Li}}^{4+} + 3\mathrm{Li_2O}$$

- **niobium vacancy model**: niobium vacancies and niobium antisites (niobium atoms) concur to compensation:

$$\langle \mathrm{LiNbO_3} \rangle \longrightarrow 4V_{\mathrm{Nb}}^{5+} + 5Nb_{\mathrm{Li}}^{4+} + 3\mathrm{Li_2O}$$

Which of these process prevails is still an open research, but the first one seems to be discredited by density measurements [17], which instead support the second model. Indeed substitutional niobium atoms introduce donor and acceptor levels in bandgap, giving rise to the photovoltaic and photorefractive effect in the absence of extrinsic impurities.
Even more important is the possibility of doping with extrinsic defect. This is a quite easy procedure on lithium niobate, thanks to its concentration of vacancies. Dopants can be added both during the grown process or in a second time with standard doping process, like thermal diffusion or ion exchange. Multiple properties can be change with doping: Fe or Mg can enhance or reduce photorefractive effect respectively, Ti is used to produce waveguide (more detail in 1.3), Er to realize integrated laser sources [18].

1.1.3 Physical properties

Optical properties

Lithium niobate is a transparent crystal with negligible absortion coefficient from 0.35µm to about 3.5µm. It's characteristic optical property is birefringence caused by anisotropy of the permittivity tensor, which is represented in orthohexagonal cell reference framework as a matrix 3x3 in equation 1.1.1.

$$\bar{\bar{\epsilon}} = \begin{bmatrix} \epsilon_{11} & 0 & 0 \\ 0 & \epsilon_{22} & 0 \\ 0 & 0 & \epsilon_{33} \end{bmatrix} \tag{1.1.1}$$

Two indices of refraction can be defined, depending on the orientatation of electric field: ordinary one $n_0 = \sqrt{\frac{\epsilon_{11}}{\epsilon_0}}$ (electric field long z-axis of the crystal), extraordinary one $n_0 = \sqrt{\frac{\epsilon_{33}}{\epsilon_0}}$ (electric field parallel to optical axis).

Both indices are function of composition and wavelength, which are described in a good approximation by the generalized Sellmeier equation 1.1.2 [19]:

$$n_i^2 = \frac{A_{0,i} + A_{1,i}(50 - C_{Li})}{\lambda_{0,i}^{-2} - \lambda - 2} + A_{UV} + A_{IR,i}\lambda^2 \tag{1.1.2}$$

where $i = \{i, e\}$, λ is expressed in nanometers and A are intensity factors which describe influence of various oscillators responsible listed in table 1.1. Equation 1.1.2 is valid in a range of wavelengths $\lambda = 400 \div 3000$nm and for composition of $C_{Li} = 47 \div 50$mol% to an accuracy of 0.002 in n_i. Both indices are strongly depended on extrinsic impurities, and this feature makes lithium niobate an easy manipulating and flexible optical material.

Parameter	Ordinary	Extraordinary
A_0	$4.5312\dot{1}0^5$	$3.9466\dot{1}0^5$
A_1	$-4.8213\dot{1}0^8$	$79.090\dot{1}0^8$
A_{IR}	$3.6340\dot{1}0^8$	$3.0998\dot{1}0^8$
A_{UV}	2.6613	2.6613
λ_0	223.219	218.203
n	2.2866	2.2028

Table 1.1: *Values of parameters for the Sellmeier equation 1.1.2 at room temperature and for a wavelength of* $\lambda = 632.8$nm *(A_0 for Nb on Nb site, A_1 for Nb on Li site, A_{UV} for high energy oscillators like plasmons, A_{IR} for phonons).*

Electro-optic effect

Electro-optic effect consists in the variation of refractive index of the crystal due to the presence of electric field, according to the relation:

$$\Delta\left(\frac{1}{n^2}\right)_{ij} = \sum_k r_{ijk}E_k + \sum_{k,l} s_{ijkl}E_kE_l + \dots \tag{1.1.3}$$

where $\Delta\left(\frac{1}{n^2}\right)_{ij}$ is a second rank tensor, describing change in the relative permittivity. In equation 1.1.3 only first 2 order are expressed: third rank tensor r_{ijk} caused a linear effect, called Pockel effect, while fourth rank tensor s_{ijkl} quadratic effect, called Kerr effect. In lithium niobate the dominant effect is only the Pockel one. Kerr effect is not negligible only for an applied field above 65kV mm^{-1} [20].
Tensor r_{ijk} for lithium niobate is expressed by matrix:

$$r = \begin{bmatrix} 0 & -r_{22} & r_{13} \\ 0 & r_{22} & r_{13} \\ 0 & 0 & r_{33} \\ 0 & r_{42} & 0 \\ r_{42} & 0 & 0 \\ -r_{22} & 0 & 0 \end{bmatrix} \tag{1.1.4}$$

where:

	r_{13}	r_{22}	r_{33}	r_{42}
m V^{-1}	$8.6\dot{1}0^{-12}$	$3.4\dot{1}0^{-12}$	$30.8\dot{1}0^{-12}$	$28.0\dot{1}0^{-12}$

Table 1.2: *Values of coefficients of the Pockel's tensor 1.1.4, data taken from [21]*

This property is extremely important for telecommunication applications and integrated optic of lithium niobate. Multiple devices with integrated fibers use this effect to change the phase of the signal, in order to realize optical switcher or modulators. Specially Mach-Zehnder interferometer is one of the device used as modulator, where through electric field, signal can be properly modulated [22]. As it will be discussed in chapter 2, a lot of articles can be found about Mach-Zehnder interferometer in $LiNbO_3$ used as a modulator, but noone about optofluidic applications.

Piezoelectricity

It possible to induce polarization through an applied stress to $LiNbO_3$:

$$P_i = \sum_{j,k} d_{ijk}\sigma_{jk} \tag{1.1.5}$$

where stress is described by a second rank symmetric tensor σ and d (third rank tensor) is usually called piezoelectric tensor, meaning the response in polarization of the piezoelectric material to a stress. In the case of $LiNbO_3$, thanks to its symmetry, independent components of d are reduced to 4:

$$d = \begin{bmatrix} 0 & 0 & 0 & 0 & d_{15} & -2d_{22} \\ -d_{22} & d_{22} & 0 & d_{15} & 0 & 0 \\ d_{31} & d_{31} & d_{33} & 0 & 0 & 0 \end{bmatrix} \tag{1.1.6}$$

Tensor d describes also vice versa effect: when crystal shows a strain under the application of an external electric field:

$$S_{ik} = \sum_{i} d_{ijk}E_i \tag{1.1.7}$$

In $LiNbO_3$ this effect is effectively exploited to induce surface acoustic waves(SAW), which are useful in Microfluidics to move droplets [23].

Pyroelectric effect

Lithium niobate exhibits pyroelectric effect: a spontaneous polarization is provided through a change of the crystal temperature. Relation between these two parameter is linear:

$$\Delta P = \hat{p}\Delta T \tag{1.1.8}$$

Where $\hat{p}$ is the pyroelectric tensor and for $LiNbO_3$ has the form:

$$\hat{p} = \begin{pmatrix} 0 \\ 0 \\ p_3 \end{pmatrix} \tag{1.1.9}$$

With $p_3 = -4\dot{1}0^{-5}\,\mathrm{C\,m^{-2}\,K}$ [24]. $p_3 \neq 0$ is physically explained by movement of Nb and Li atoms along z-axis caused by temperature.

As other properties, even pyroelectric effect has application in field of microfluidics. Some application have been published recently about manipulation and trapping of droplets, heating crystal selectively generate electric field, which can trap particle on surface [25, 26].

Photovoltaic effect

Photovoltaic effect is typical of non-centrosymmetric crystals. In these material momentum of photo-excited electrons has preferential direction. So when crystal is exposed to light, a stationary density of current is generated:

$$j_{PHV,i} = \beta_{ijk} e_j e_k^* I = \alpha k_{G,ijk} e_j e_k^* I \tag{1.1.10}$$

where β_{ijk} is photovoltaic third-rank tensor, which can be defined as the product between absorption coefficient α and the Glass coefficient k_G; e_j and e_k are the polarization vectors of the incident light wave and I its intensity. In $LiNbO_3$, the direction of this current is mainly long to the optical axis since $k_{G,333}$ and $k_{G,322}$ are more than one order higher than other direction ($k_{G,333} = 2.7\dot{1}0^{-9}\,\mathrm{cm\,V^{-1}}$, $k_{G,322} = 3.3\dot{1}0^{-9}\,\mathrm{cm\,V^{-1}}$, $k_{G,222} = 0.3\dot{1}0^{-9}\,\mathrm{cm\,V^{-1}}$).

Photorefractive effect

Materials showing both electrooptic effect and photovoltaic, such as $LiNbO_3$ have another phenomenon called photorefractivity, which derives from presence of both. It consists in the change of index of refraction of the material through illumination. Light excites electrons in donors level, which change state up to conduction band. If crystal is illuminated with non uniform pattern, excited electrons move through crystal to dark regions in order to be trapped by acceptors (by diffusion photogalvanic effect or by drift). After electrons movement, crystal is characterized by non-uniform charge distribution, which leads to internal space-charged electric field. Thanks to electrooptic effect, internal electric field changes the refractive index. Then illumination pattern can therefore provide recording of refractive index pattern.

Both intrinsic and extrinsic impurities with two valence states add this necessary intermediate donors levels in the band. In $LiNbO_3$ the role is cover by niobium antisite Nb_{Li}, which can be found both in donor state Nb^{4+} or in acceptor state Nb^{5+}. Effect can be also enhanced through Fe doping, which introduces external impurites with two valence states: Fe^{2+}, Fe^{3+}.

1.2 Microfluidic channels in Lithium Niobate

Microfluidic is the science about controlling, manipulating and studying of small volume of fluids in range from microliter down to picoliter. It is characterized by low value of

Reynolds number Re [1] and laminar flow are established in this range. On these conditions no mixing happen and control of fluids is gained. The possibilities of controlling and studying small fluid amount have importance not only for the study of fluid dynamics at small range itself, but also for wide range of applications from chemistry to biology. In fact extreme control of small amount of fluids represent perfect environment for biology sample or chemical reactions. These features give growing relevance to the Microfluidics in last years.
Droplet microfluidics have a lot of interest thanks to the realization of small isolated volume. Droplet, which fluids is usually called dispersed phase, flow in channel space out by immiscible fluid usually called dispersed phase. Droplets have typically volume of Microfluidic mention before. In the most general case, Microfluidic droplet circuit is made by different shapes of microchannels with typical dimension of droplets. These sizes force fabrication processes to have high precision. New study of polymeric material such as PDMS or PMMA provides the necessary precision. Because of this, Microfluidic success has been grown simultaneously with studies on new polymeric material. In fact usually Microfluidic device are made from these material thanks to their reproducibility and quite easy manipulation. Thanks to photolitography techniques microchannels circuit are realized with good precision [27, 28]. Nevertheless these material are not always eligible to have high level of integration. Moreover in many cases they can swell with oil based fluids, or can be damaged from solvent. In last year new material have been proposed for Microfluidic Application: Lithium niobate [11, 29, 30, 31]. In this section it is presented Microfluidic circuit realized in a substrate of $LiNbO_3$. The circuit is composed with a T-junction droplet generator and microchannels of 50µm nominal width and height. Performance of T-junction in $LiNbO_3$ is already checked by same author of this thesis. So for a complete review about applications on lithium niobate with care to fabrication and characterization it is recommended [11].

1.2.1 Droplet Generator: T and Cross junction

There many methods to generate droplets in microfluidic channel. In general generators need to guarantee high reproducibility, high range of frequency flowing droplets and low dispersion in volume of droplets. Necessary device for a droplet generator are pumps, which inject both phases in the Microfluidic circuit. Generators, which involve more external energy source than pumps like mechanical valves or external electric field, is usually called active, while others passive.

[1] Reynolds number indicate the ratio between inertial and viscous forces, $Re = \frac{\rho \mu L}{\eta}$ where: ρ is density of fluid, μ mean velocity, L linear dimension of the flow and η is fluid dynamic viscosity.

For this work thesis, T-junction and cross-junction droplet generators have been used. Both of them are passive generator and use simple junction shape between microchannels. Cross and T-junction are a particular geometry of channels, working as a droplets generator. In the first case two channels cross each other orthogonally shaping a crosswise junction as name suggest. In the same way, in second case, two microfluidics channels are crossed to form a junction between channels with T shape. Both junctions work similarly, in fact cross-junction with one extremity closed acts as a T-junction. In the following only T-junction theories will be briefly discussed . Later advantage of cross-junction will be reported.
In T-junction droplets can be generated flowing two immiscible fluids in channels. Typically in Microfluidics droplet liquid is called continuous phase, while other dispersed one. Different working regimes are discovered varying important parameters such as physical properties of fluids (density $\rho_c\rho_d$, viscosity $\eta_c\eta_d$, surface tension and wettability properties such as angle of contact) and fluxes Q_cQ_d (with obvious reference to continuous and dispersed phase). 3 different well-define regime are:

- **Co-flow**: two phases flow in half of channel simultaneously and no droplet are produced. This regime is supported by small velocities, fluid with similar viscosities and if fluids present both high wettability with channels surface.

- **Dripping**: On the contrary respect first one, in the dripping regime the droplet are formed at T-junction. In this regime droplets can fill completely channel walls (unless thin film of dispersed phase) or not. The first case is called squeezing regime. Thanks to its stability, in most of the cases this is favourite regime.

- **Jetting**: it is an in-between regime. Indeed droplets are generated after little portion of channels, where two phases coflow. This regime is characterized by high frequency.

Independently of regime droplets are produced thanks to the forces exerted by continuous phase on the dispersed one entering main channel. Forces involved are related to the capillary, drag and pressure contributes. Different theories are under investigation about the process and possible regimes, which can emerge. The best fitting theory of experimental data in [11] is Christopher *et al* [32]. As authors suggest, breaking point starts when these three forces balance each other:

$$F_\sigma + F_\tau + F_p = 0 \tag{1.2.1}$$

- **Capillary force**: it is given by the difference between Laplace upstream and downstream of droplet(with approximation of curvatures), multiplied by the area of interface bh:

$$F_\sigma \sim \left[-\sigma\left(\frac{2}{b}+\frac{2}{h}\right)+\sigma\left(\frac{1}{b}+\frac{2}{h}\right)\right] bh = -\sigma h \tag{1.2.2}$$

- **Drag force**: it is the force generated due to viscous shear applied from continuous phase flowing on the emerging dispersed phase. These authors approximate shear stress rate with average velocity of continuous phase u_c divided by gap size between wall and tip of droplet $w_c - b$ (see figure 1.4).

$$F_\tau \sim \eta_c \frac{u_c}{w_c - b} bh = \eta_c \frac{Q_c u_c}{(w_c - b)^2} \tag{1.2.3}$$

- **Squeezing pressure force**: this force is obtained from a lubrication analysis [33] for the pressure during flow in a thin gap with aspect ratio $(w_c - b)/b$.

$$F_p \sim \Delta p_c bh \sim \frac{\eta_c u_g a p}{w_c - b} \frac{b}{w_c - b} bh = \frac{\eta_c Q_c b^2}{(w_c - b)^3} \tag{1.2.4}$$

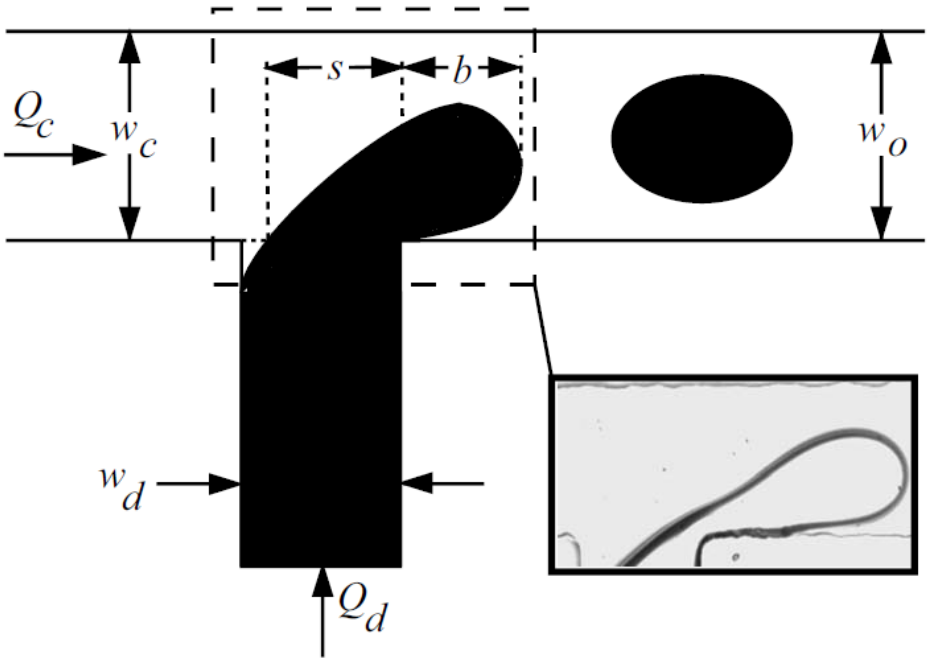

Figure 1.4: *Schematic diagram of the emerging droplet taken from the paper of Christopher et al [32].*

From equation 1.2.1 and approximation listed before author derive law of for droplet length and frequency. Christopher found that they depend on $\phi = \frac{Q_d}{Q_c}$ and Ca^2. He calculated the droplet length before the neck starting shrinking through 1.2.1. Than he added the additional length during neck shrinking, which he approximate as $u_{growth}\dot{t}_{squeeze}$, where $t_{squeeze} \approx \frac{w_d}{u_c} \approx \frac{w_d w_c h}{Q_c}$ and $u_{growth} = \frac{Q_d}{bh}$. Length normalized to w_c was derived as a result of some easy algebraic passage:

$$\bar{L} = \bar{b} + \frac{\Lambda}{b}\phi \tag{1.2.5}$$

where $\bar{b} = \frac{b}{w_c}$ and $\Lambda = \frac{w_d}{w_c}$. With similar arguments they derived also the semi-empirical trend for frequency for constant value of ϕ:

$$\bar{f} = \frac{\eta_c w_c}{\sigma} f \propto Ca^{1-\delta} \tag{1.2.6}$$

where, in fact, $1 - \delta$ is determined experimentally to be 1.31 ± 0.03. This 2 laws are also verified experimentally for a T-junction in $LiNbO_3$ by same author of this work [11].
In this thesis it has been observed that the best configuration is given by a cross-junction with one inlet closed for using it as T-j. Nevertheless same theoretical studies can be used. The choice of cross-junction was dictated from the possibility of new working regime. Indeed cross-junction can work with two different fluid as dispersed phase (injected in two opposite channels), with the consequently adding of different droplet regime and configuration. This feature of crosswise circuit opens new application such as one showed in [34].

1.2.2 Microchannels realization on Lithium Niobate

Recent application of lithium niobate in Microfluidics highlights lack of studies about fabrication process of microfluidic channels. Many different micro-fabrication techniques have been reported in the past for optics application such asr idge waveguides, but no reference about hundreds micrometers structures. Only articles found in literature about this theme are wrote by Chauvet *et al.* [35, 36] and Pozza *et al.* [29].
Tests and many attempts have been done in order to realize channels directly on lithium niobate. The primary goal is optical quality of lateral surface of channels with prospective of waveguides integration. The starting point of tests was the fabrication attempts of microfluidic structure on silicon and glass. In literature the best results were obtained by adaptation

[2] $Ca = \frac{\eta_c u_c}{\sigma}$ Capillary number is a very important parameter of microfluidic, it represents ratio between viscous shear stress and capillary pressure.

of common process used in microelectronics for silicon, such as chemical etching and micromachining, and in optics for glass, such as femtosecond laser damaging. Possible solutions are:

- **Chemical Etching**: it is usually used for ridge waveguides on $LiNbO_3$ [37], thank to its chemical stability. Process consists in a bath of hydrofluric acid solution, which etches the surface of sample with rate between 1 and 0.06 µm h^{-1} depending on crystal cut. This rate makes this technique too slow to have application, even if optical quality is reached. Feasible application is Opto-Nanofluidics structure.

- **Reactive Ion Etching**:it consists in etching of samples with plasma of reactive ions. In case of $LiNbO_3$ plasmas successfully used are SF_6, CF_4 and CHF_3. Results reported in [38] are rate up to 50nm min^{-1}. Same similar technique are used in [39] with Inductive Coupled Plasma at rate of 190nm min^{-1}. Micrometer structures with optical quality are achievable with these rates waiting hours, but specific facilities are needed.

- **Focused Beam lithography**: As the name suggests, the sample is etched with focused ion beam. Heavy ions are usually used in this technique differently from electron beam in order to have more resolution (heavier particles have higher momentum, less wavelength so less diffraction). Typical roughens of surfaces are at submicrometre length scales [40]. Although this quality etching rate around 10 nm makes this technique more appropriate for Nanofluidic approaches.

- **Laser Ablation**: it is the process of removing material from a surface by irradiating it with laser beam. it is popular for fabrication of optical waveguides [41, 42]. Possibility to design almost any 2D pattern make it perfect not only for optical waveguided circuits, but also Microfluidic ones. Furthermore engraving depth can finely controlled, and it is an already widely used technique in lithium niobate for different purposes (from index changing to waveguides design). Some tests of 200x100 µm channels with this technique have been realized [29]. However this technique require specific facilities and bottom surface of channels present stripes in correspondence to laser scan.

- **Mechanical Micromachining**: it is not a specific technique, but series of them. In general a micromachining process use mechanical technique to manipulate material at scale of micrometer. Most Interesting for Microfluidic structure building are micromechanical drilling and milling, which are commonly used to engrave opto-electronics silicon device. Lack of results for lithium niobate is attributed to risk of damaging and

breaking. Nevertheless recent improvement in micromachining technology allow some astonishing test of fabrication on lithium niobate like [43] and [31]. In the first of these references cylindrical hole with diameter of 500µm on $LiNbO_3$ have been engraved with CNC milling machine. While in the second one 200x100µm microchannels have been realized with good lateral surface quality. This last result will be analysed better later and some additional results will be reported in this work for less sizes.

Diced Microchannels

Microchannels for the device of this thesis is realized by micromachining dicing with DISCO DAD 321 precision saw. The technique is quite fast and have wide range of possible size for channels, still maintaining good surface quality, which are demonstrated in this section. Dicing have been done thank to collaboration with university of France-Comté, Besançon (France). DISCO DAD 321 mount circular polymeric blades with diamond particles. Two different blades are tried for 2 different size of channels: in table 1.3 all specifications are reported.

Diameter [mm]	**Thickness**[µm]	**Rot. speed** [rpm]	**Cut. speed** [$mm\,s^{-1}$]	**Width**[µm]	**Depth**[µm]
56	200	10000	0.2	200	100
56	50	10000	0.2	50	50

Table 1.3: *Parameters of the 2 blade used for realization of two different microchannels on lithium niobate. Rot. stay for Rotating and Cut for cutting. Depth and Width are referred to nominal values of channels size. For both blades sample have been keep clean during dicing with water flow.*

After cut sizes of microchannels have to be measured, in fact in table 1.3 only nominal width and depth are reported. For checking channels it have been used optical microscopy and atomic force microscope (AFM) for the quality, while for measure depth and width profilometry. One typical result of profilometry analysis for both size of channels are showed in table 1.4.

channel	$\bar{h}$[µm]	σ_h [µm]	$\bar{w}$ [µm]	σ_w [µm]
50x50	46	1	55	1
200x100	98	1	205	1

Table 1.4: *Result of profilometry measurements: average of 10 different profiles (4 in short channel of cross and 6 in long one) both for height $\bar{h}$ and width $\bar{w}$. σ is referred to the mean error: $\sigma = \frac{standarddeviation}{\sqrt{N}}$* [3].

Images reported in figure 1.5 are obtained with Eclipse Ti-E, Nikon with a plan 10x/0.10 objective and profile with surface profilometer KLA Tencor P-10. Profilometry results show a considerable difference between nominal value and effective one 1.4. However the precision from this point of view is not always a restricted requirement, at least it is not for this work's device.

More important are surface profiles and in general quality of dice. In this way topology measurements are performed by Veeco Cp-II AFM in contact mode (see figures 1.5e, 1.5f). Also a morphology studies have been done with Gwyddion data analysis software, with which roughness of surface are calculated for both typology of channels and resulted: 6.8 $\pm$ 0.5nm for lateral surfaces and 19 $\pm$ 6nm for bottom one. These values highlight the efficiency of technique, considering also low time of fabrication. For these reasons all microfluidic stage of this thesis' device are made with this method.

Only one drawback of micromechanical dicing is the constraint on the channels geometries: T-junction is not a viable option, as Cross-junction is. However As demonstrated later and seen before cross-junction can work as a T-junction too.

Chip sealing

In order to complete chip and finally close engraved channels a gastight covering is needed. Two different solutions have been tried: first one is the simplest, but provides worse microfluidic performance. In both cases cover have been realize with microscope slide silica which were put in contact with proper vise. Same adhesive polymer have been used the Norland Optical Adhesive 68 (NOA68) by Norland Products Incorporation. It is a liquid photopolymer which becomes 100% solid after curing under UV light at $350 \div 380$ nm. Difference is in the gluing phase where glass were stucked on $LiNbO_3$ substrate.

First solution consists in putting NOA68 only all around glass, while thin layer between silica and $LiNbO_3$ is filled by hexadecane. Filling with liquid provides some problem for Microfluidic performance. Thin layer is not easy to be completely filled by hexadecane, a lot of little air bubble stick into the layer, making pressure inside the channel unstable.

To avoid this problem another solution is studied:

[2]Standard deviation refers to $\sigma = \sqrt{\frac{\sum_{i=1}^{N}(x_i-\mu)^2}{N-1}}$ where μ is mean, x_i is data and N is total number of data.

[3]Standard deviation refers to $\sigma = \sqrt{\frac{\sum_{i=1}^{N}(x_i-\mu)^2}{N-1}}$ where μ is mean, x_i is data and N is total number of data.

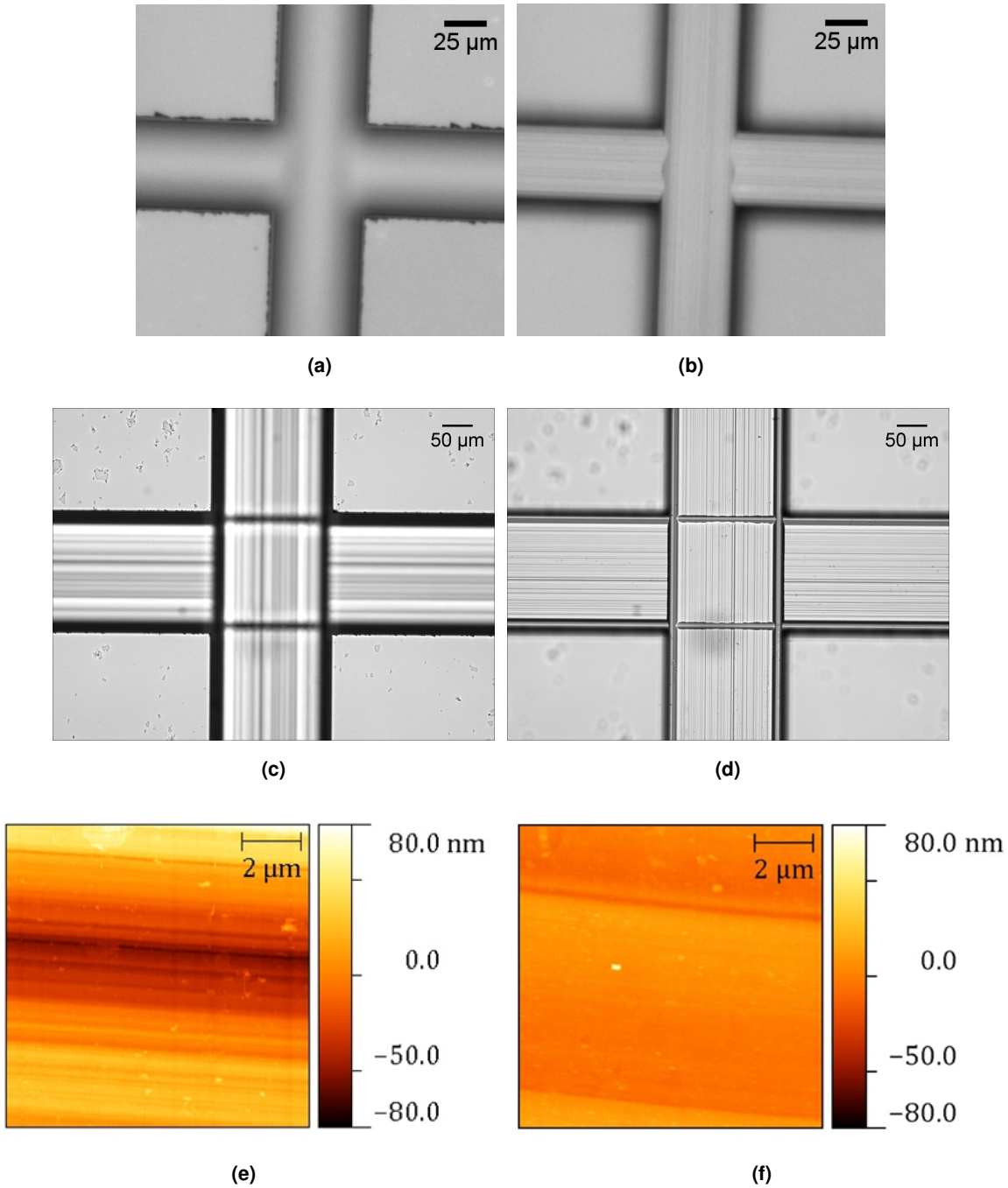

Figure 1.5: *Characterization of the microfluidic channels engraved on $LiNbO_3$ with dcing saw DISCO DAD 321. In 1.5a and 1.5b are reported images of the top and bottom edges the 50x50 channels respectively taken with optical microscope. In 1.5c and 1.5d same images for 200x100 channels. 1.5e, 1.5f 10x10 μm^2 AFM images of the bottom and the side of the channel respectively.*

1.2.3 Lithium niobate wettability

As mention before, one of the most important parameter which influenced working regime of T-junction is wettability of fluids on the channels surfaces. It depends on microscopic interaction between surface and fluids. Since both physical-chemical properties of molecules of fluids and microscopic morphology of surface are involved, it is not easy to characterize wettability in any situation.
One of the most diffused measure in Microfluidics to analyse wettability is static constant angle CA between interface solid-fluid of small droplet on the surface in air. From this angle wettability coefficient k can be derived from Young's law [44] as shown in figure 1.6.

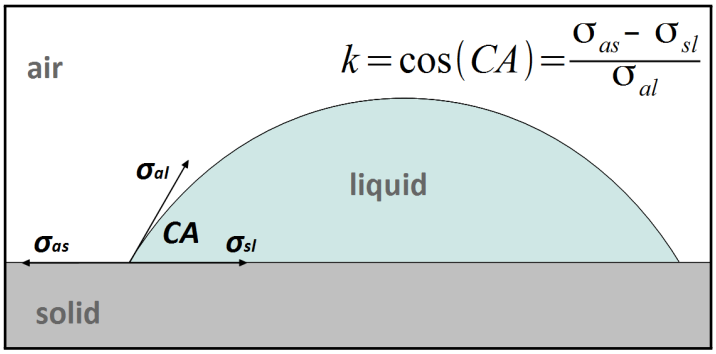

Figure 1.6: *Sketch of contact angle CA, σ_{al} σ_{sl} σ_{sa} indicate surface tension between air-liquid, solid-liquid and solid-air. On the right Young's law is represented, where k is wettability coefficient.*

As seen in figure 1.6, higher is contact angle lower is the wettability and vice versa.
In order to achieve squeezing regime continuous phase have to wet all surface, have to be immiscible with dispersed phase and thin film have to surround droplet. Typical application in biology of droplet microfluidic suggest that aqueous solutions have to be used for dispersed phase. According to these facts, usually a good choice for continuous phase is oils such as hydrocarbons, silicone or vegetable oils. In this work it is decided to use two of most common liquids in droplets Microfluidics: Hexadecane and Water (for more detail see section 3.1). A detailed study of wettability of these fluids on lithium niobate is provided by Bettella in [30]. Author deposited liquid droplets of 500 nL on surface of lithium niobate, he take picture varying all possible setting respect optical axis of crystal. For every setting more than 10 droplets are measure, mean of contact angle are reported in figure 1.7.

From Bettella's analysis lithium niobate exhibits a moderate hydrophobicity, CA of $62 \pm 1°$, and high oleophilicity, $CA < 10°$. However lithium niobate can not comparable with standard Mircofluidic polymers CA around 100°. This value can only reach with functionalization process, which can also normalise wettability of 4 channels surfaces.

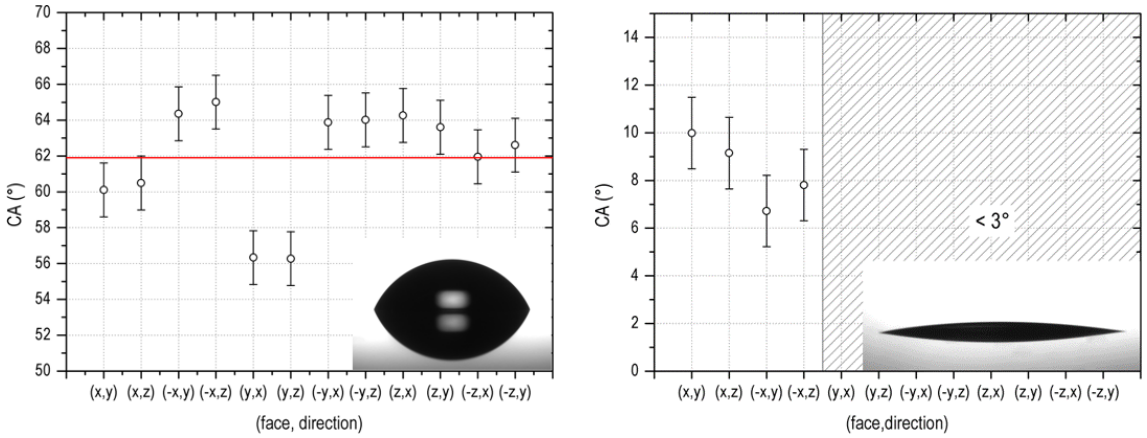

Figure 1.7: *Contact angle (CA) measurements from [30] on lithium niobate surface for different crystal and different crystallographic directions for water 1.7a and hexadecane 1.7b. The red line represents the average of all CA determinations.*

OTS functionalization

A solution of octadecyltrichlorosilane (OTS)[4] in toluene at concentration of 100µM have been flow in the channels. As Bettella explained, OTS molecules bond with surface oxygen atoms resulting in a Self Assembled Monolayer of OTS, which is orientated with long hydrocarbon chains on the centre of channels. Hydrocarbon Tails of molecules exhibits high hydrophobicity, resulting in changing of wettability.
As previous measure for CA, same procedure have been used for functionalized lithium niobate (see figure 1.8) with resulting CA of $101 \pm 1°$for water and $35 \pm 1°$for hexadecane. To better figure importance of functionalization and in general wettability in droplets Microfluidics, tests have been done of flowing with or without OTS in T-junctions. Difference are clearly highlighted 1.9.

1.3 Integrated Optic in Lithium Niobate

1.3.1 State of the art

Lithium niobate is well-known material in the field of integrated optic applications. His optical properties (see section 1.1) and very low optical absorption ($\sim 0.1\,\mathrm{dB\,cm^{-1}}$) make him perfect candidate as the substrate for devices like waveguides, electro-optical modulators and

[4]ocatadecyltrichlorosilane: $CH_3(CH_2)_{17}SiCl_3$; CAS number 112-04-9; Mm=387.93g mol^{-1}; density 0.984g mL^{-1}

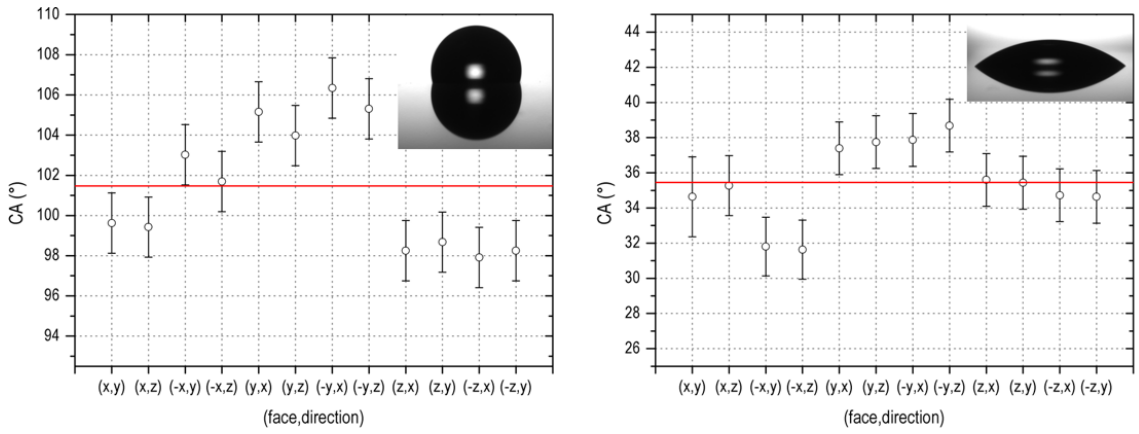

Figure 1.8: *Contact angle measurements from [30] on lithium niobate surface for different crystal cut and different crystallographic direction after funtionalization with a solution of OTS in toluene at concentration of 100 μM, for water 1.8a and hexadecane 1.8b. The red line represents the average of all CA determinations.*

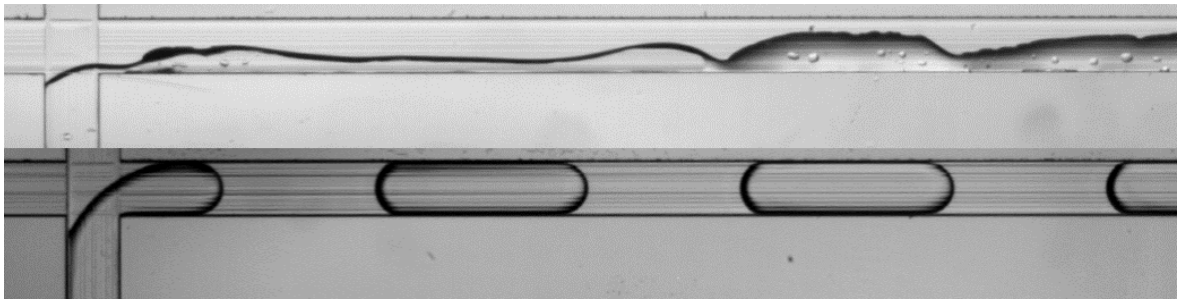

Figure 1.9: *Effect of the functionalization on the production of droplets. On the top co- flowing after functionalization, while the same channels with OTS are represented. Both images are took from [30].*

switches, nonlinear optical frequency converters and diffraction grating. The first building block in any optcial device is the realization of waveguides on $LiNbO_3$. Different techniques are available for fabrication of waveguides.

Titanium In-diffusion

Titatinium in-diffusion is most popular technique for waveguide realization in $LiNbO_3$ since mid-seventies[45]. Its wide use derives from its simplicity, flexibility and good result in light confinement along both extraordinary and ordinary axes. Moreover Titanium in-diffusion preserves electrooptical property [46], which guarantee the realization of optical switchers and modulator like Mach-Zehnder interferometer [22].

Proton-Exchange

Proton-exchange is another well-known technique for waveguides fabrication. Refractive index change is obtained by immersion of $LiNbO_3$ in a liquid source of hydrogen ions (usually benzoic acid or toluic acid) at temperature $150 \div 400$ [47]. H^+ substitute ions of lithium in the crystal. An annealing treatment is required to prevent optical damage and complete Annealed Proton Exchange (APE). Comparing this technique to previous one show that with APE higher change of index of refraction can be reached($\Delta n_e \approx 0.1$). Disadvantages are mainly connected to the spoiling of the electrooptic effect and that only modes polarized on extraordinary axis survived.

Ion-Implantation

Ion implantation consists in the bombardment of crystal with ions. When light elements are implanted, the net result is a damaged crystal surface with change of refraction index of order of 0.1 [30]. Ions are implanted with fixed energy and fixed incidence angle, resulting in both the generation of point and extensive defects in first microns below surface. Variety of ions (H, B, C, O, F, Si, P, Ag) at different energies (from 1 MeV up to more than 20 MeV) and fluencies ($10^{12} \div 10^{17}$ ions/cm^2) have been reported [48, 49, 50]. Change of index strongly depend by material, ion and nuclear interaction [51]. Damaged crystal need post-annealing process to recover optical transparency and to consolidate ion implantation. Comparison with other techniques confirm that Ion implantation can achieve higher refraction index change in both axis even with particular geometry, but it requires expensive and huge facilities.

Laser writing

Laser writing consists in the refractive index change with photorefractive effect and structural modification. In first case small Δn can be reached (order of 10^{-3}) with focused laser beam [52]. Higher intensity of laser source implies more efficiency in term of Δn, but also more risks of optical damage on the crystal.
In second case Δn can be obtained damaging irreversible crystal structure with femtosecond pulsed laser. Waveguiding region is between two damaged section. Indeed with this technique both n_e and n_o can be decrease. Change in refraction index depend strongly on the energy of the beam [53].
Main advantage of laser writing is the capability to realize of a 3D bulk waveguide, but on the other hand efficiency in term of Δn is poor.

Ridge Waveguides

Last technique of this brief review is realization of ridge waveguide. This particular waveguides are different form others realized in previous methods. Thin layer on the surface of the crystal is removed in order to leave only a ridge waveguide surrounded on 3 side by different material (most of cases air). Two kind of process are typically used for fabrication of these waveguides: mechanical micromachining [54] and chemical etching [37]. The first one consists in the ablation of surface through micro-saws or micro-mills, which can ensure surface with optical quality. Machines have to be numerically controlled by computer. Instead chemical approach is simpler, crystal is plunged in a hydrofluoric acid bath.
Ridge waveguides show high confinement provided to high refractive index differences between crystal and surrounding material. Nevertheless fabrication defects can have higher dispersion than diffused waveguides due to scattering.

1.3.2 Titanium Diffusion

Waveguides in this work are realized via titanium diffusion, fabrication method is described in detail in 2.3 and all problem derived from MZI geometry during titanium diffusion. In this section Titanium diffusion in lithium niobate is analysed more deeply. In general case metal diffusion of thin layer inside oxides is well described by Fick's Law:

$$\frac{\partial C(x,t)}{\partial t} = \frac{\partial}{\partial x}\left(D\frac{\partial C(x,t)}{\partial x}\right) \tag{1.3.1}$$

where $C(x,t)$ is the dopant concentration, while D is diffusion coefficient, that can depend on both temperature and concentration. Usually the temperature dependency is modelled by

exponential law according to Arrenhius theory: $D = D_0 e^{-\frac{E_a}{k_B T}}$ where E_a is activation energy. More complicated is dependency on Concentration, indeed if D depend on C, solution is not so straightforward with all boundary conditions. Analytical solutions have been discovered in the past in case of two inter-diffusing semi-infinite alloys [55].

Considering D independent on C, the most studied cases are two different type of solution: one describes the diffusion at constant temperature, if the thin film of metal is not completely diffused, while the other one describes the same situation but with exhausted film. The first solution approximates residual film during diffusion as an infinite source of dopant, so concentration at interface metal-oxides is considered saturation one C_s. The solution is described by an error function $C(x,t) = C_s erfc\left(\frac{x}{\sqrt{4Dt}}\right)$. Second solution approximates the thin metal layer with negligible width at $t = 0$, which mean $C(x, t = 0) \neq 0$ only for $x = 0$. With reflection boundary condition, the solution of Fick's Law has a Gaussian profile $C(x,t) = \frac{M}{\sqrt{\pi Dt}} e^{-\frac{x^2}{4Dt}}$, where M is total amount of dopant deposited in the film.

In the case of this thesis, titanium waveguides need to be completely diffused. In order to achieve this goal, thin layer of titanium have to be diffused for enough time to exhaust itself. Simple Gaussian shape can be used to fit diffusion profile along the direction perpendicular to the surface. A lot of studies have been made on titanium in-diffusion in $LiNbO_3$ because of its wide use in integrated optics. Three steps have been recognized during titanium diffusion:

- $T \sim 500$°Ctitanium to TiO_2;
- $T >$600°Closs of lithium correspond to epitaxial crystallites of $LiNb_3O_8$;
- $T >$950°Ca $(Ti_0 \cdot 65\, Nb_0 \cdot 35)O_2$ mixed oxide source appears and it acts as diffusion source for titanium in-diffusion inside the bulk crystal.

CHAPTER 2

Mach-Zehnder Interferometer

Since 70's one of most used modulator in Telecommunication services is Mach Zehnder interferometer (MZI), that can be even realized in integrated optics by way of suitable geometries of waveguide on monolithic substrate. In the first section 2.1 of this chapter it is overviewed the state of the art of the design for a low-loss waveguided Mach-Zehnder Interferometer. This configuration is the building block of a novel configuration of an optofluidic Lab-On-a-Chip developed in this work. From the knowledge on the theme, the optimal MZI geometry for Optofluidic's chip is derived 2.2. Then in section 2.3 is described the fabrication process of MZI on lithium niobate.

2.1 Low-loss waveguided Mach-Zehnder Interferometer

Mach-Zehnder interferometer (MZI) is an interferometer where a beam is divided in 2 arms that are later recombined on a well defined path. Peculiarity of this kind of interferometer is that two beam travel only once on two different well-separated optical paths, as shown in figure 2.1.

MZI configuration can be integrated on a single substrate in integrated optics by exploiting electrooptic effects. This feature makes this device highly configurable and with a various applications. One of this is for electro-optic modulator in fibre-optic communication, in most of the cases MZI is integrated in waveguide in monolithic circuits.
In literature there are a lot of work about this MZI used as optical modulator [22] for fiber-

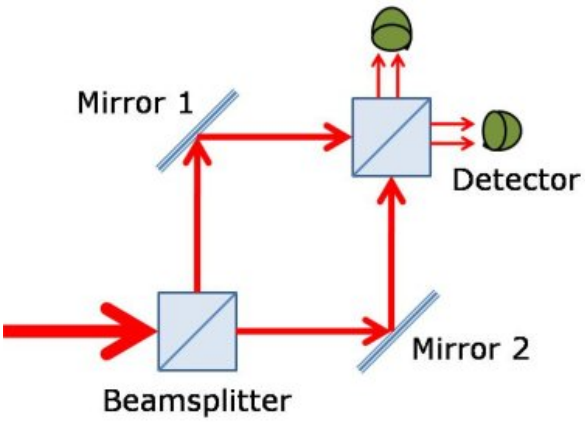

Figure 2.1: *Example of Mach Zehnder interferometer, two beams are splitted from a single source, than these two travel only once on well-separated optical path and then recombined to interfere.*

optic transmission system mostly on $LiNbO_3$ due to his property. This kind of device is typically used in telecommunications, where optical signal is modulated through local change of index of refraction thanks to electrooptic effect (Kerr effect [56]) and electric field. This change in index of refraction usually is applied on one of two arms, in this way changing index of refraction cause a phase shift of beam in that arm. Consequently Phase shift is connected with applied electric field through law described in section 1.1 in case of $LiNbO_3$. In this way interference of two arms, and so the output of MZI is controlled with electric shift. Due to this application waveguided integrated MZI in $LiNbO_3$ is one of the most studied device from the born of fiber-optic telecommunications. In this work only the low-loss geometry and the optimal design for our device are investigated, without studying deeper electrode configuration and their coupling with MZI, because this study is beyond the aim of this thesis. MZI realized for Optofluidic device of this work is similar in geometry and configuration to those used in telecommunication. This section describe the study of the optimal geometry for the device from state of the art in low-loss integrated MZI on $LiNbO_3$.

In the design of a waveguided MZI there are some elements to take into account for a low-loss device. A part from the same problems observed for a straight waveguide. MZI needs 2 Y-branches as represent in figure 2.2, both junctions have a tapered transition from single waveguide to Y. In the design of waveguided MZI, in fact there are 4 main parts, which characterize the optical signal and can provide loss:

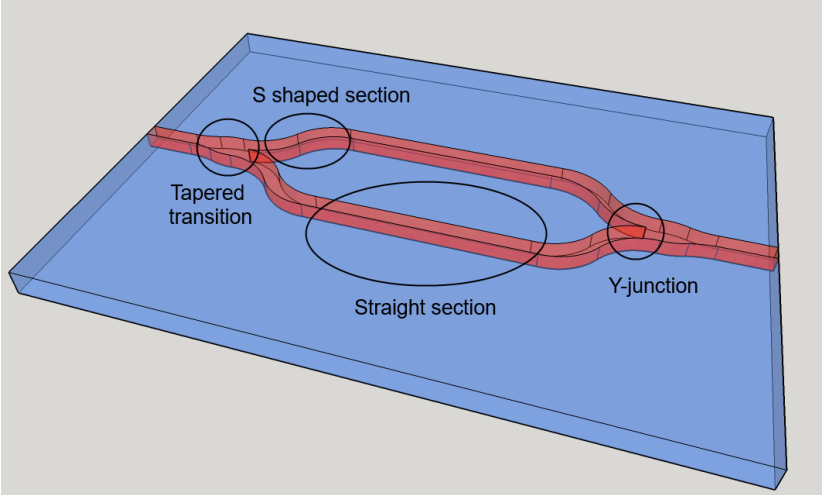

Figure 2.2: *Example of Mach Zehnder interferometer integrated in waveguide, two beams are splitted from a single source through a Y junction, than two arms are made by S shaped transition and straight section. Typically the arm with phase shift is called signal arm, while the other is called reference one.*

- angle of y-branch: difference between mode and power splitting;
- Y-junction and tapered transition;
- bending loss;

These critical issues are discussed in literature both from the theoretical and experimental point of view, in order to reach the optimal configuration for Optofludic application.

2.1.1 Angle of y-branch: difference between mode and power splitting

Y-branches in waveguide are a key geometry for the design of an optical circuit. Therefore there are already a plenty of articles about this from 70s, which study from more theoretical point of view [57], others have more experimental approach [58]. Y-branch, in fact, can work as beam splitter [59] or as mode splitter [60]. Indeed the control of few geometric parameters allow to easily split the beam in intensity or in mode. Burns and Milton have studied a lot these topics [61]. Before introducing their work, a brief overview on the properties of optical stage of this work's chip needed for the device will be presented.
For the design of MZI it is needed a low loss Y-branch for maximizing intensity, but also the same mode propagation on the two arms. The easiest mode to choose is zero-order one because it is symmetrical. In fact, zero-order mode on the output can guarantee the best coupling with external fiber coupling. Moreover one of the aim of this work is to understand

better how light and droplet interact, the simplest way to proceed is to start with simple output of the guide.

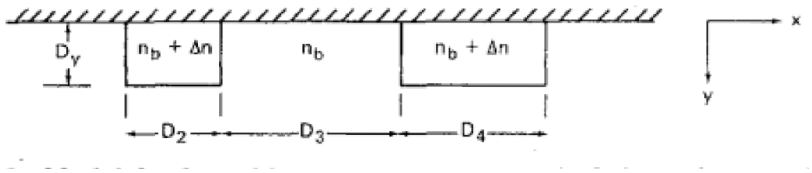

Figure 2.3: *Section scheme of two arms near Y-junction. Image has been taken from article [62]*

As guaranteed by the zero order spatial distribution Burns and Milton developed an analytical solution for mode coupling in Y branches in [62]. They consider local normal modes, which are modes characteristic of the entire cross section of the structure. For the case of two separated guiding region see figure 2.3 (the two arms after Y-junction), they express the transverse field dependence of the first two local normal i, j as superposition of transverse field dependences of the modes of the 2 guide considered separately. Than they consider the propagation of Amplitude of A_i and A_j along the direction of guide (z):

$$\frac{dA_j}{dz} = C_{ij}\frac{dD_3}{dz}A_i - i\beta_j A_j \tag{2.1.1a}$$

$$\frac{dA_i}{dz} = -C_{ij}\frac{dD_3}{dz}A_j - i\beta_i A_i \tag{2.1.1b}$$

where β is the propagation costant of the mode, D_3 is the distance between the guides, $C_{ij}\Delta D_3$ represents the overlap integral between local normal modes i and j (see figure 2.3. These equations have solutions for particular branching shape. The necessary shape is described by:

$$2\tan\left(\frac{\theta}{2}\right) = \frac{dD_3}{dz} = \frac{\gamma\Delta\beta_{ij}}{C_{ij}} \tag{2.1.2}$$

where γ is an arbitrary constant and $\Delta\beta_{ij} = \beta_i - \beta_j$. From this basis, some approximations and coupled-mode theory REF authors deduce that the transition boundary for power divider can be described approximately as:

$$\frac{\Delta\beta}{\theta\sqrt{\beta_0^2 - n_3^2k^2}} \ll 0.44 \tag{2.1.3}$$

where n_3 is index of refraction in the section between guides, k is wave vector, θ is branching angle and β and $\Delta\beta$ is the same parameter mention before, for zero and first order. In this work's MZI $\theta \to 0$

2.1.2 Low loss Y-junction and tapers in integrated optic

Every integrated MZI need Y-junction and every Y-junction contains tapered transition. In this way the calculation of radiation loss of these geometries is fundamental for a low-loss design of MZI. Baets and Lagasse in 1982 published their works about these topics [63]. They calculated the light propagation through various simple geometries of integrated-optic tapers and Y-junctions. They used numerical method, which is a combination of beam propagation and the effective refractive-index method. In particular they consider a waveguide geometry sketched in figure 2.4.

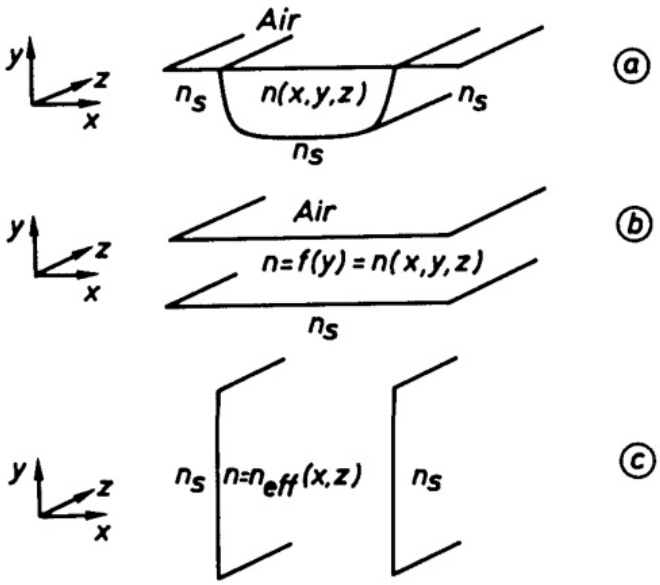

Figure 2.4: *a) Sketch of original waveguide, b) slab waveguide used to calculated the effective refractive index, c) resulting 2D effective profile, image has been taken from [63]*

Than they wrote the equation for wave propagation inside waveguide as:

$$\nabla^2 E_x + k^2 n^2(x,y) E_x = 0 \tag{2.1.4}$$

However they did not solve directly this 3D equation with beam propagation method, but first they reduced into a 2D equation with effective-index method, thank to the small dependency of *n(x,y,z)* from *z*. Indeed effective index method [64] consists of replacing *n(x,y,z)* for any value of x and y by $n_{eff}(x,y)$.

For tapered configuration they calculated the output power of the fundamental mode, if input mode is only fundamental, as:

$$T_{00} = \left| \int_{-\infty}^{+\infty} \phi_{in}(x)\phi^*_{out}(x)dx \right|^2 \tag{2.1.5}$$

First Baets and Lagasse developed their model for abrupt transition. Equation 2.1.5 is computed by authors for different steps indices, and their result for is illustrated in figure 2.6.

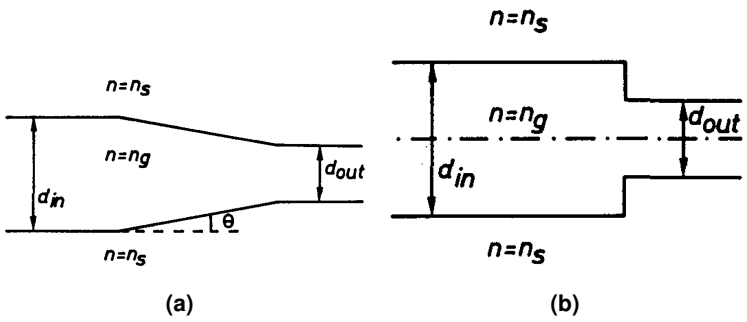

Figure 2.5: *Waveguide transition where n_g is effective index: a)abrupt transiton, b) tapering transition, images have been taken from [63]*

As picture 2.6 shows, T_{00} is dependent only on the normalized widths:

$$V_{in} = kd_{in}(n_g^2 - n_s^2)^{\frac{1}{2}} \tag{2.1.6a}$$

$$V_{out} = kd_{out}(n_g^2 - n_s^2)^{\frac{1}{2}} \tag{2.1.6b}$$

where parameters are clear presented in figure 2.5. The results show a minimum for $V_m = (V_{in}V_{out})^{\frac{1}{2}} \sim 2.5$.

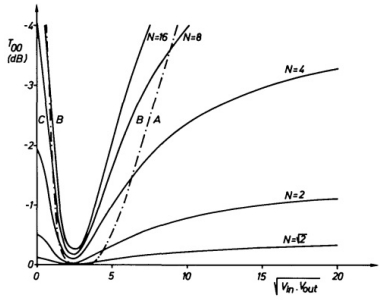

Figure 2.6: *Power transfer in abrupt transition for different value of N, region A input output multimode, region B input multimode output single, region C last possibility, image has been taken from [63]*

In case of tapering transition (see fig. 2.5) T_{00} radiation loss depend on V_m, $N = \frac{V_{in}}{V_{out}}$ and $\sin(\theta_{eff}) = \frac{\sin(\theta)}{NA}$. For this thesis N=2 is interesting case because input guide of Y-junction has

same width of each two output arms, in order to maintain same order in all MZI. So only result reported in figure 2.7 is for N=2. As shown in the graph, choosing V_m between 1.5 and 4 a loss less than -0.5dB is guaranteed.

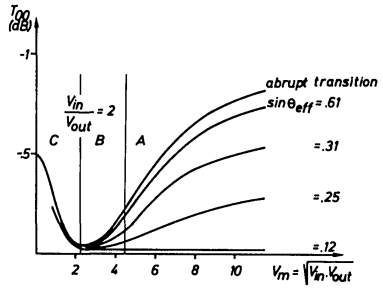

Figure 2.7: *Radiation loss of tapering transition varying V_m and θ_{eff}, region A,B,C are te same of previuos figure, image has been taken from [63]*

In same article of tapered region [63] Baets and Lagasse computed also the radiation loss of the Y-junction varying its geometry. They take the same approach for tapered transition, for simplicity they report only the result for different shape and not all discussion. Some of their geometries is not interesting for the aim this work, like non symmetric Y-branch or with one arm broke off. For this reason it will be presented interesting results. Figure 2.8a illustrates the particular geometry for this computation, while in figure 2.8b is reported the estimation of loss varying both angles. This graph suggests to choose an angle until 1°.

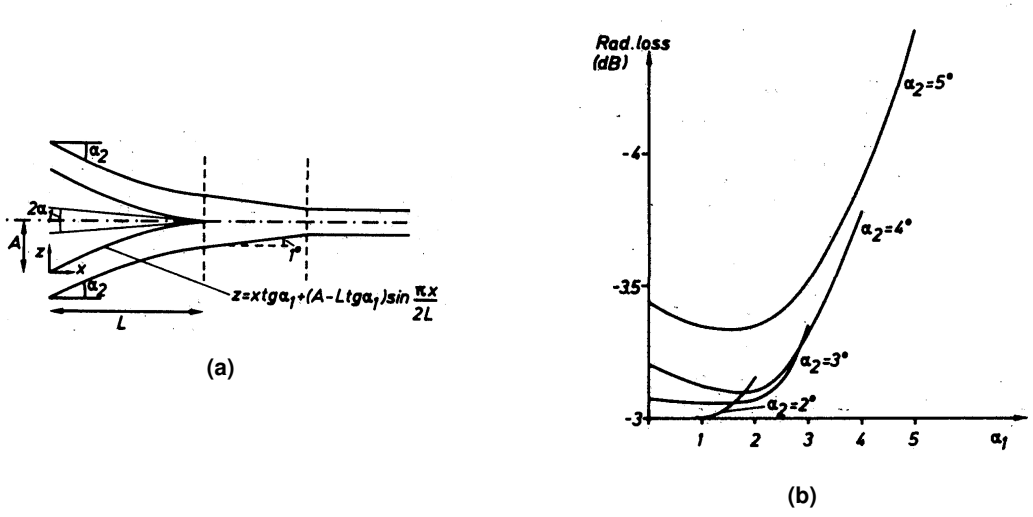

Figure 2.8: *a) Geometry for Y-junction considered in [63], b) result for computation for geometry in (a) varying both angle.*

2.1.3 Bending loss

Many authors have investigated the radiation loss in a bending waveguide, with various geometries and methods. Several types of solutions have been developed for circularity bent guides.
MZI needs bent guides to connect Y-junction to the straight parallel arm. Different shape for bend can be choosen. In [65] a brief review of state of the art on the bending loss is given and some computation for guide with varying radii of curvature. Authors investigated in particular S-curved bends (see fig. 2.9).

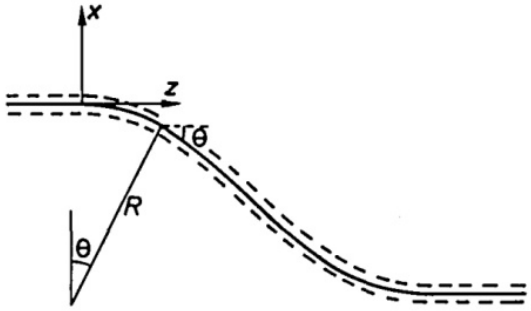

Figure 2.9: *Arbitrarily S-shaped bend guide, image has been taken from [65]*

In most general the bending loss can be write as:

$$\int_{bend} \alpha_0(R) ds \tag{2.1.7}$$

where $\alpha_0(R)$ is the bending loss per unit length of a bend with constant radius of curvature. With similar methods to the previous section Authors computed loss for 4 different shape of S-bend. For every of these shape they calculated radiation loss varying W and L, where W is total extension of S in x direction and similarly L long z (see fig. 2.9). Four shapes design from these authors are presented in the following equations:

$$x(z) = \frac{W}{2}\left(\cos(\frac{\pi z}{L}) - 1\right) \tag{2.1.8a}$$

$$x(z) = \frac{W}{2\pi}\sin\frac{2\pi}{L}z - \frac{W}{L}z \tag{2.1.8b}$$

$$connection\ by\ two\ arcs\ of\ a\ circle\ with\ radius : \pm\frac{L^2}{4W}\left(1 + \frac{W^2}{L^2}\right) \tag{2.1.8c}$$

$$a\ suboptimal\ curve\ R_0\ (\theta)\ design\ from\ author\ (see\ [65]) \tag{2.1.8d}$$

The radiation loss for all of them are calculated varying W for fixed value of L. the result are reported in graph 2.10.

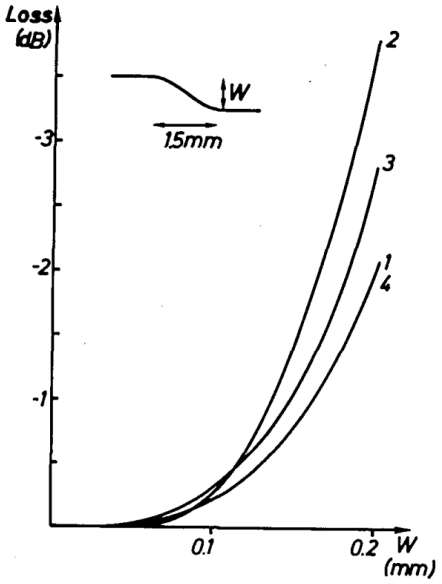

Figure 2.10: *radiation loss for four different S shape 1 refer to 2.1.8a, 2 2.1.8b, 3 2.1.8c, 4 2.1.8d, image has been taken from [65]*

2.2 Design of integrated Mach-Zehnder interferometer for droplet sensing

Finding optimal geometry of MZI for this thesis device is extremely important. In fact not only simple fiber coupling is needed, but also MZI geometry have to respect the constraints of droplet and channel width. Channel crossed orthogonally both arms of MZI, which cause non-negligible optical loss. These losses, added with that from waveguides, dictate to reduce to the lower value bending and more in general designing loss. Indeed design of critical part of MZI (see 2.1) have to provide radiation loss negligible compared to guide fabrication loss. Another key aspect of the design is the distance between the arms that have to be compared with droplet length: four different regimes of optical signal are expect confronting distance between . For this reason this distance has to be choose in order to reach both regimes taking care of droplet lengths.

In order to achieve these goals in this thesis a geometry for device was studied and described starting from design issues presented about MZI crux parts in section 2.1. As mentioned before, MZI has two Y-junctions (both with 2 tapered transition) and four S-shaped waveguides. In this case device does not need particular geometry different from symmetric one, so all S are equal to each other and the same hold for Y.

The first step is the proper design of the waveguides. As suggest Montevecchi in [34] waveg-

uides, realized with titanium in-diffusion 1.3 in $LiNbO_3$, width of 5µm can provide mono mode, but also is enough large for minimizing imperfection from realization process 1.3. In order to guarantee mono-mode also in arms of interferometer, both Y-junctions of MZI has to act as a power splitter 2.1. For this reason we designed Y with angle less than 3°. This choice is sustained also from low-loss radiation. However this choice is only about design and this is not correspond to real size due to imprecision in fabrication method. Specially in section 3.2 fabricated guide are characterized and compared with designed ones.

What already discussed in section 2.1, tapered transition provides some radiation loss. For this MZI, referring to 2.1, $V_m = (V_{in}V_{out})^{\frac{1}{2}} = 4.7$ (see section 2.3 values of index of refraction) as pictured in graph 2.7, T_{00} is less than -0.5dB for any value of θ, even abrupt transition. Nevertheless to be sure to reduce as much as possible the loss, tapered transition was designed with length L_t = 0.2 mm (see figure 2.11 for better following discussion about parameters). Instead of L_t, W_t is fixed because have to be exactly double of the width of the channel W_t =10µm (all parameters are sketched in figure 2.11 where final design is represented.). With these values resulting angle is 2.8°.

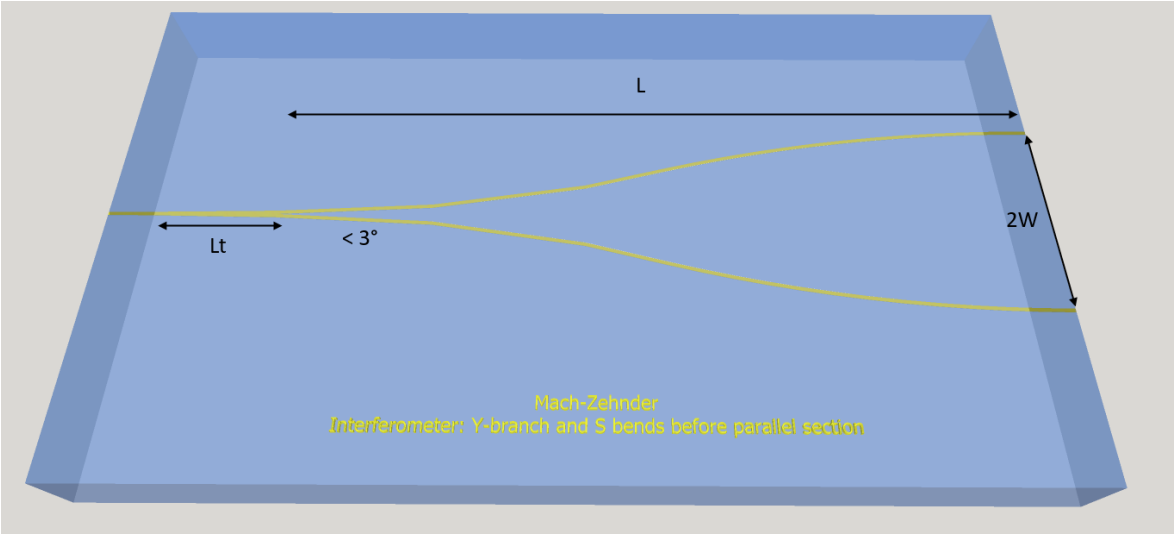

Figure 2.11: *Sketch of the Y-branch and S bend just before the parallel arms section.*

Similar discussion hold also for influence the design of S guide. The simplest shape for the photolithografy is the connection by two arcs of a circle with radius $\pm\frac{L^2}{4W}\left(1+\frac{W^2}{L^2}\right)$ (see section 2.1 for parameters). As reported in graph 2.10, radiation loss is less than -0.5dB for L = 1.5mm and W < 0.1mm. The choice of L depends only in saving space on the chip, but dimension of integrated MZI is negligible compared to space reserved to microfluidic channels. On the contrary W depends on distance between arms, which is fundamental

parameter for the reason mentioned before. Indeed the comparison of droplets lengths and distance between interferometric arms changes radically output signal. Droplet produced from T-junction 1.2 have length that change from around one time to five times channel width. For this reason the distance chosen for W is 130µm, which can provide low radiation loss in bend guide and both working regime of device, considering microfluidic channels width is 50 µm. Last parameter to fix is L, but instead L it simpler fix radius of both circle composing S, because L has no particular designing constraints and Mask writing machine can engrave easily curves with precise value of R. So R was fixed to 20 mm, which implies a $L = 3.2$ mm. In figure 2.11 the sketch of the final design is reported. This is only a theoretical picture of MZI, later when MZI is realized, they can have different values due to imprecision of fabrication process. For this reason real MZI needs a complete analysis and characterization, which is reported in next section.

2.3 Fabrication and Characterization

Fabrication method of waveguided MZI have to guarantee good quality to waveguide: low loss, no interruption and mono-mode, but also geometries of MZI 2.2 before have to strictly follow the design. From fabrication process listed in 1.3 the optimal one is titanium diffusion. Indeed titanium indiffusion is one of the most used technique for integrate optics in lithium niobate.
Many steps are required for fabrication:

- sample cutting of desired dimension;
- photolitography for designing geometry of waveguide circuit;
- titanium deposition via sputtering;
- lift-off of residual photoresist;
- termal diffusion of titanium;
- polishing and lapping;

To simplify understanding of all the process In figure 2.12 are sketched step by step fabrication process.

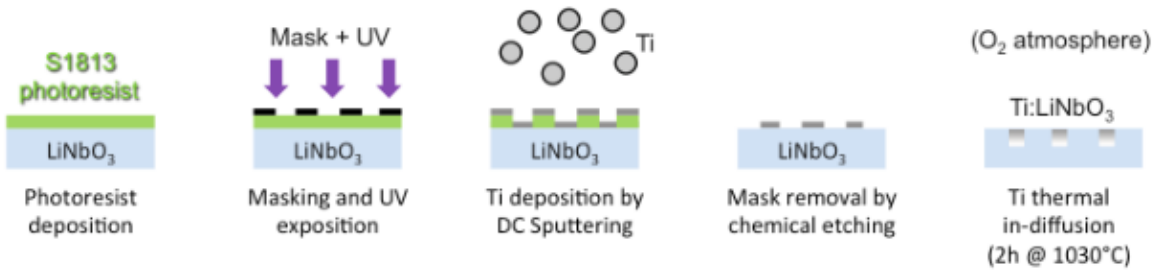

Figure 2.12: *Sketch of the main steps for the fabrication of the channel waveguides by titanium in-diffusion.*

Sample cutting

Samples were cut from a commercial x-cut wafer of congruent $LiNbO_3$(crystal Technology) with a thickness of 1 mm. X-cut sample are chosen because x-cut is the one with lowest loss waveguides. Blade used for cuts is a diamond-coated Cu-alloy blade. Cutting machine is a South Bay 540 with a graduated protractor, which allows perfect alignment of the wafer. Indeed alignment is important in order to know the direction of crystal axis respect to shape of the sample.
Second step after is Photolitography, which include distribution on the samples surface of a plastic viscous material called photoresist through spinning samples. Thick of remaining layer of photoresist depend on velocity of spin and samples shape. For this reason, wafer circular shape can provide better uniformity of layer than typical samples, which typical are rectangular. During testing of all fabrication, cutting was always the first step, while for the final devices cutting have been left as last step. Indeed photolitography on all wafer ensures a higher reproducibility.

Photolitography

Photolitography consists in three steps: coating of photoresist, exposition under UV lamp with proper mask and developing. All these processes have to be performed in clean room to avoid any particles on surfaces. Clean room used in this work is an ISO 7 financed by MISCHA project (Microfluidics laboratory for scientific and technological applications).

Photoresist employed is S1813 from Microposit S1800 G2 series, some tests have been done with similar photoresist belonging to same series with Profilometer KLA Tencor P-10. These kinds of photoresists are developed for micro-litography on silicon, but they have been showed working also with $LiNbO_3$. Tests are performed with 2 positive photoresists S1813 and S1805, which are compatible with emission spectrum of the available UV lamp.

Differences between the two consist in the aspect ratio of the interface between photoresist layer and cleaned surface (with coating procedure). In fact Profilometry study gives that the mean height of layer is 1.14 µm and 0.30 µm for S1813 and S1805 respectively. Considering that titanium sputtering provides 30 nm of Ti and maximum width of channels is 10 µm, S1813 can guarantee a precise and clean lift off procedure thanks to its height respect to titanium one, its nominal resolution of 0.48µm and the sharpness of the wall in interface.
Before coating, samples are all covered with primer based on hexamethyldisilizane (HMDS) to favour adhesion of S1813 to lithium niobate surface. Primer is then coated to 200rpm for 30s before a coating of photoresist of 6000rpm for 60s. Various values rpm were tried in order to reach uniformity of layer height.
After coating, exposition is needed to fix desirable geometry with mask cover. Mask containing the design of MZI as reported in2.2 has been realized by specialized company (Delta Mask B.V.) with chromium layer of 980Å patterned with laser on a plate of Soda Lime glass. Samples was aligned and put in deep contact with mask, than exposition at UV lamp last 18s and intensity of UV lamp is 9mWcm^{-2}. The final step is the developing process: samples with layer of photoresist is dipped in bath of Microposit MF-300 of 60s, than washed in distilled water.
Thin layer of photoresist has been checked before the sputtering how accurately exposed photoresist can follow design. Instruments employed to measure thickness of this layer is same Profilometer used to for characterization of photoresist layer and Microscopy Eclipse Ti-E, Nikon with 40x apochromatic objective. Profilometry checked not only the precision with which design, described in section 2.2, is followed, but also real width of holes, where guides will be situated.

Example of results for one MZI is reported in table 2.1, graph 2.14 and image 2.13. From profilometry result that error of measurements are completely negligible respect to the difference between measured point and theoretical one (red point and green line in 2.14)) due to the fabrication imprecisions. To estimate the fabrication resolution Root-mean-square deviation[1] have been calculated between experimental data and theoretical profile $f(x) = 5.97 + \frac{5.97}{170}x$ considering as width of the stripes. The estimation results 0.32 µm, which is value comprehensible considering nominal value of photoresist resolution 0.48µm.

[1]Root-mean-square deviation: used measure of the differences between experimental values predicted by a model $RMSD = \sqrt{\frac{\sum_{i=1}^{N}(y_i - y_{Model})^2}{N}}$. It can be used in this case because model law is not predicted from data itself.

[2]Standard deviation refers to $\sigma = \sqrt{\frac{\sum_{i=1}^{N}(x_i-\mu)^2}{N-1}}$ where μ is mean, x_i is data and N is total number of data.

[3]Error of the mean refers to $\frac{\sigma}{\sqrt{N}}$

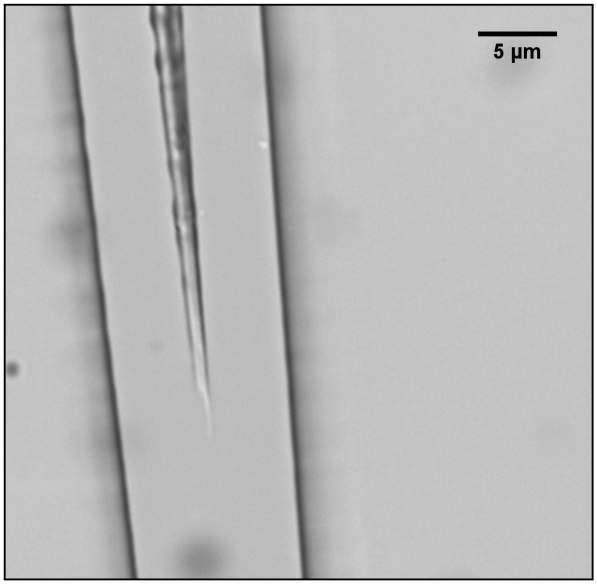

Figure 2.13: *Image took by optical microscopy Microscopy Eclipse Ti-E, Nikon with 40x apochromatic objective coupled with Fast camera Phantom VRI v7.3. Despite some imprecision in the spike, photoresist strictly follows the Mask design.*

	Mean[µm]	**Standard deviation**[2] [µm]	**Error of mean**[3] [µm]
left arm	5.92	0.21	0.05
right arm	6.00	0.17	0.04
weighted mean	5.967	-	0.001
distance between arms	260.3	2.6	0.6

Table 2.1: *Example of result of profilometry measurements of one MZI. Distance between arms refers only to parallel section.*

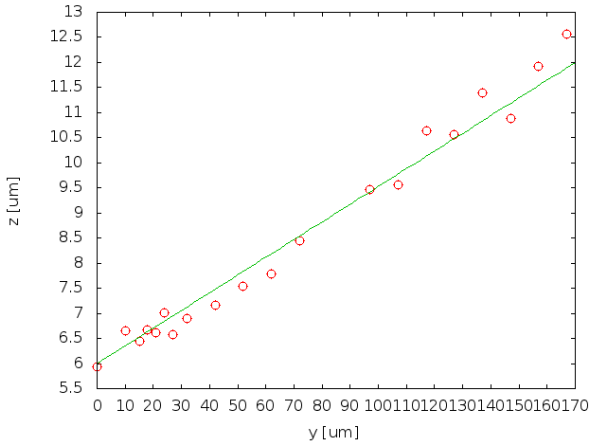

Figure 2.14: *Red points represent width of photoresist holes measured with Profilometer KLA Tencor P-10. Instead green line is trend of the designed profile of tapered zone considering width stripe as measured in 2.1. Axis labels are referred to the crystal ones. Measurements errors are negligible respect to the contribution deriving from fabrication, for this reason errors are not reported. An estimation of the contribute from the fabrication is described in this section.*

As show values in table 2.1 the width of waveguides results wider than Mask, probably due to diffraction during exposition to UV light. Instead of width of holes for guides shape of MZI seems to be accurately designed during exposition: parallelism of arms is respected as the distance between arms and moreover, Graph 2.14 highlights also how accurately profile of tapered section are followed by photoresist layer.

Titanium sputtering

Titanium deposition is performed in magnetron-sputtering, which bombards the samples with ions of a plasma. Plasma is sustained by a potential difference between target and source of titanium in a vacuum chamber at controlled pressure of Argon atmosphere, which feeds the plasma. The potential difference is supplied by settable continuous current. Moreover magnetron sputtering is provided by permanent magnets, with aim to confine secondary electrons coming from the collisions between plasma ions and target. The consequence of this is an increasing of cationic density near target, which results in higher sputtering rate. For this thesis work sputtering machine used is from Thin Film Technology. Vacuum set up have two stages: rotatory pump, which can reach pressure around $8 \div 9 \cdot 10^{-2}$ mbar and a turbomolecular pump, which can keep pressure below $3 \cdot 10^{-6}$. After putting samples inside the chamber and reach vacuum grade mention before, Argon gas was injected in the chamber. Flow is controlled by a feedback system, which guaranteed a constant pressure

of $5 \cdot 10^{-3}$mbar. Finally titanium target was connected to DC power supply with 40 W, but for the first 3 minutes it was kept covered by a shield, which allows to remove impurities and oxidized layers on surface of the target. After this presputtering time, a sample holder aligned surface samples in direction perpendicular to titanium trajectories. Some test about sputtering time have been done. Results showed that for about 30 nm, optimal quantity for necessary diffusion, is about 22 minutes.

Lift-off

S1813 masked with layer of titanium is removed with process called lift-off. Sample is dipped in a bath of SVC(TM)-14 at temperature of 60°Cfor the several minutes. This is the key process of all methods, if photoresist does not dissolve in right way some piece of residual titanium can drop and stick on $LiNbO_3$ surface . Moreover, if the UV lamp exposition is uncorrected, thin layer of photoresist could be remained under the stripe of titanium, which has to diffuse in the crystal.
For these reasons, before the diffusion process, samples have to be checked accurately with the optical microscope and Atomic force microscope (AFM). This control is not only useful for checking quality of lift-off, but also how good is precision of the MZI geometries fabrication. Specially spike in-between Y-junction(see section 2.2) is key factor for optical loss. As Sasaki report in [66], if spike is cut due to fabrication imprecision, optical loss in the junction increase depending on distance $2s$ between arms at junction, see figure 2.15a. Results of theoretical calculations about loss of this imprecision is reported in figure 2.15b by Sasaki.

Images taken by same optical microscope used before is reported in figure 2.16. This picture highlights the titanium Y-branch of MZI, which well follows design described in section 2.2. Despite residual photoresist in-between two arms close to the Y, parameter s described by Sasaki results at least 10 times less than width of the channel, avoiding every risk of loss from that particular even after diffusion. These photos are useful not only for checking the quality of reproducibility in the designing of MZI, but also for checking if the protocol of preparation did not follow the right step during lift-off and potentially clean sample and repeat fabrication before diffusion. In fact before diffusion stripes of titanium are removable through a bath in NaOH and samples become easily reusable.

For more precise values and analysis AFM Veeco Cp-II AFM in contact mode is used (for information about technique of Atomic Force Microscopy [67]). This instrument can

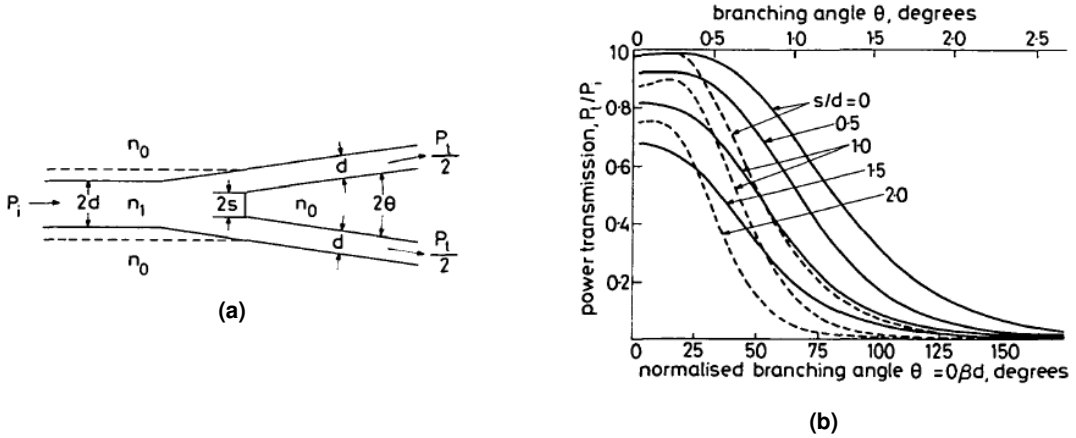

Figure 2.15: *Sasaki's studies about particular Y-junction geometry in 2.15a: in 2.15a it is pictured sketch of the Y-junction with imperfect spike between two arms, in 2.15b power loss due to s part is reported, dotted and full lines are referred to different width of guides. . Both images have been taken from [66]*

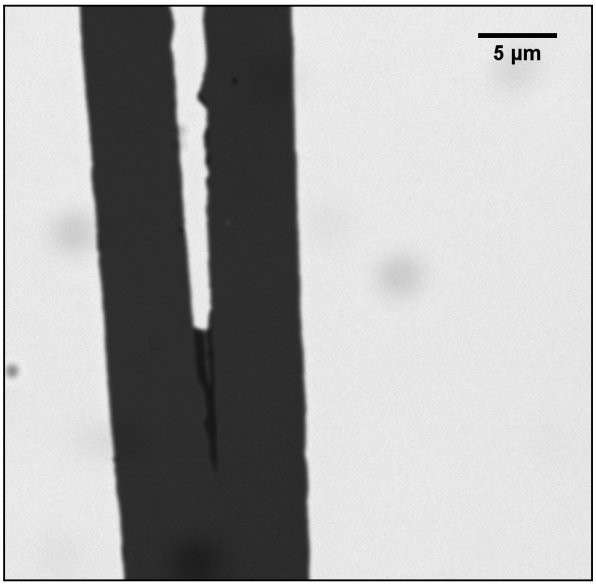

Figure 2.16: *Image taken by optical microscopy Microscopy Eclipse Ti-E, Nikon with 40x apochromatic objective coupled with Fast camera Phantom VRI v7.3. Despite some imprecision in the spike as already observed for photoresist in 2.13, titanium stripes strictly follow Mask design.*

measure with more precision the stripes size and so give more informations than Microscope and Profilometer about results of lift-off. Example of one analysis is reported in 2.17a where typical images from instrument are represented. MZI's Y and Tapered zone are illustrated and through Gwyddon data analysis software three different section profiles have been measured in graphs 2.17b results are reported. These data stricly followed size of Mask profile and Photoresist circuit as expected. Furthermore spike between arms resulted pretty sharp, making Sasaki's expected loss entirely negligible.

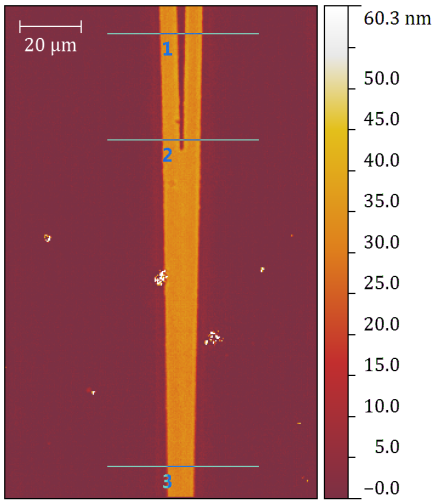

(a)

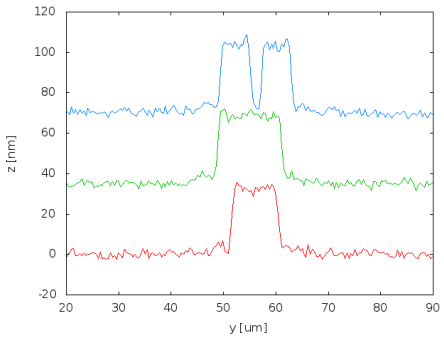

(b) 1=blue, 2=green, 3=red

Figure 2.17: *Example of the Atomic Force Microscope analysis result for MZI's Y-junction and Tapered section before diffusion of titanium. White semi spherical object in pictures are residual dust on surface of the sample. Profile in 2.17a refer to corresponding profile studied in 2.17b. For a better representation profile 2 and 3 have been shifted long ordinate by 35 and 70* nm *respectively. Axis labels are referred to the crystal ones.*

Thermal diffusion

Diffusion is performed by the tubular furnace Hochtemperatureofen Gmbh (model F-VS 100-500/13) by Gero. Samples are put in the centre of the oven with a quartz rod and there they are diffused for 2h at 1030°C. Heating and cooling rates have to be controlled, in order to avoid crystal stress, because of property of $LiNbO_3$ (see section 1.1). So the heating rate was maintained under 300°C/h, while cooling one under -400°C/h. Oxygen has to be fluxed during process in order to reduce surface damage after titanium in-diffusion [68]. Flow rates of oxygen was set to $50\,\mathrm{NL\,h^{-1}}$. Unfortunately wet conditions were not possible in a reproducible way as needed with available set-up so that optimal conditions reported in

literature to avoid lithium out-diffusion were not reached.

Polishing and Lapping

After the diffusion process, the waveguides are finally realized, but all processes can damaged and ruined lateral surface. In this way output and input optical coupling with waveguides can be compromised. To avoid these problem, the lateral surfaces are lapped and polished with a professional polishing machine by Logitech. It works with rotating disk on which surface of the samples lay down. Good quality of surface's roughness is reached through 3 different stage: first one using iron disk wet by aqueous suspension of 9µm alumina particles, second analogous disk with 3µm particles and third with polyurethane disk wet by aqueous suspension of submicrometer particles. Nominal roughness is guaranteed by this machine is less than 1nm, it also was verified with AFM measurements.

2.3.1 RBS, SIMS and microscopy Characterization

Optical Stage of device are finally realized, but before characterize it 3.2 and coupling with microfluidic one, another deep check have been done. Titanium diffusion have been analysed with Rutherford Back Scattering (RBS) and Secondary Ions Mass Spettrometry (SIMS).

Titanium diffusion profile have been studied starting from concentration on surface. Titanium have been sputtered on glass and measured with RBS at Legnaro National Laboratories (LNL-INFN). The incident beam consist in a 2MeV proton and revelator is a silicon solid state detector, which stay at 170°respect to the beam and have a detection angle of $1.966 mrad$. Result of measurement is reported in 2.18, where a titanium film of 41 ± 5nm.

From background of Si and O derived from glass peak of Ti emerge. Data highlight that layer of Ti is partially oxidized $TiO_{0.8}$, but in thermal diffusion at temperature of 500°Call Ti oxidized in any case. Interpolation with gaussian report a surface concentration of $150 \cdot 10^{15}$atoms/cm^2.

First microns of concentration profile inside $LiNbO_3$ have been analysed with Secondary Ion Mass Spectrometry using CAMECA ims4f. Primary beam is a Cs^+ ions at 10kV, with final impact energy equal to 14.5 kV. Negative secondary ions detection have been exploited together with electron gun compensation of the charge build-up occurring in insulator.

Data of one measure are figured in 2.19, where they are normalized over the total amount of diffused titanium calculated from RBS. Since the titanium is completely exhausted by

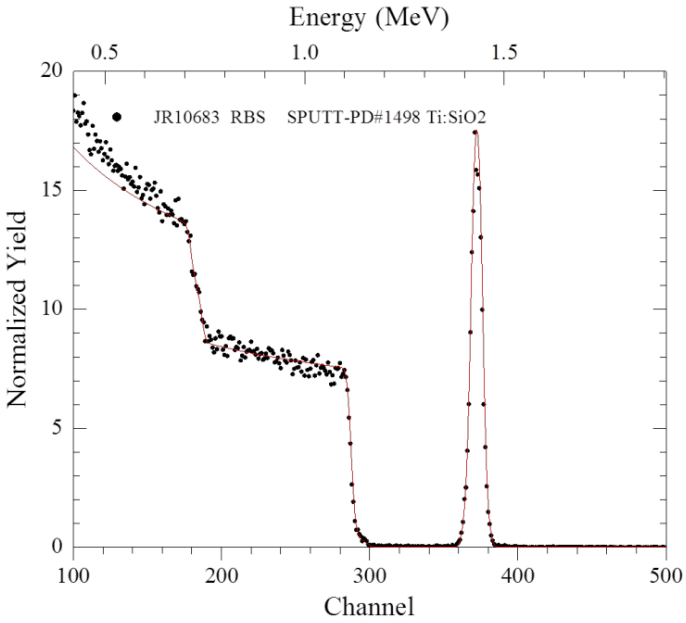

Figure 2.18: *RBS spectrum of an as-deposited sample of Ti on a silica (SiO_2) substrate.*

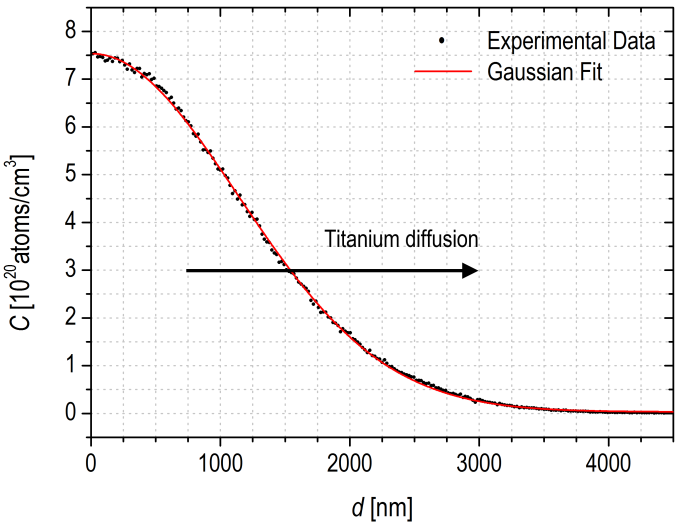

Figure 2.19: *Concentration profile obtained from the SIMS measurement of a 37±1* nm *titanium film on a x-cut $LiNbO_3$ substrate after diffusion in O_2 at 1030°Cfor 2* h.

diffusion, the Fick's law 1.3.1 as reported in 1.3 can be solved analytically and the solution is a Gaussian profile. The diffusion coefficient at 1030 and titanium concentration at the surface are derived from Gaussian fit, as mention in section 1.3:

$$D = \frac{\sigma^2}{2t} = 89 \pm 2 \frac{nm^2}{s} \qquad C_0 = 1.06 \pm 0.04 \cdot 10^{21} \frac{atoms}{cm^3} \tag{2.3.1}$$

where σ is the Gaussian standard deviation.

From concentration profile of the titanium difference in index of refraction can be calculated through empirical law according to [69, 70] as: $n_o(x,y) - n_o = \Delta n_o = K_{n_o} C(x,y)^{\gamma_o}$ and $n_e(x,y) - n_e = \Delta n_e = +K_{n_e} C(x,y)$. Results from these two equation are $\Delta n_o = 0.66 \pm 0.02 \cdot 10^{-2}$ and $\Delta n_e = 1.12 \pm 0.03 \cdot 10^{-2}$.

CHAPTER 3

Experimental Setups

In this chapter the experimental setups are presented, both for microfluidic and optical stage of the device. In particular the device is separately characterized from both microfluidic and optic points of view. In the first section 3.1 experimental setup for microfluidic measurements is presented. In the same section typical results with relative statistical analysis of droplet generator are reported. In the next section it is presented Optical setup for properly coupling to waveguides. Instead of the microfluidic stage, the optical one is more deeply characterized. Firstly straigth waveguides are optically characterized both in form and intensity of output beam. Then particular care is reserved to the optical study of Y-branch and MZI configuration discussed in chapter 2 on page 27.

3.1 Microfluidic setup and characterization

The study of microfluidic performance of cross-junction on lithium niobate have been realized with standard microfludic set-up provided by research group Lafsi in Universitá degli Studi di Padova. As discussed in section 1.2 cross-junction can work as T-junction, but also as cross with two different dispersed phase. Both of two working regimes are presented in two different application, and both need the same apparatus. Fluids are pumped into channels with 2 syringe pumps from PHD 2000 Harvard Apparatus. In case of cross-flows where three fluids are pumped, two are pumped with same flow thanks to the two available location for syringes provided by this model of pump. The PHD 2000 can work in a flow rate

range from 0.0001 µL min^{-1} to 220.82 mL min^{-1}, thanks to stepper motor, which pull plunger at fixed speed. Syringes mounted on the pumps are Hamilton Gastight series 1700, they are connected with polyethylene tubings by Deutsche & Neumann with an internal diameter of 0.5 mm and an external one of 1mm resistant to acids, bases, alcohols and salts solutions up to 80°C.

The fluids for this thesis are hexadecane [1] for continuous phase and MilliQ water for dispersed one. In the case where three fluids are used, third one details will be reported when cross-flow application are discussed. Surface tension σ between two fluids is increased adding surfactant (SPAN®80)[2] in continuous phase at 0.08% (w/w), which is above the critical micelle concentration.

For detection of droplets, a fast camera was connected to the microscope, which records image sequences of flowing droplets. Microscope is an Eclipse Ti-E, Nikon with a plan 10x/0.10 objective with a 30 mm working distance. Fast camera Phantom VRI v7.3 records images 800x600 with a calibration of 3.46 µm/px. Complete setup is sketched in picture 3.1

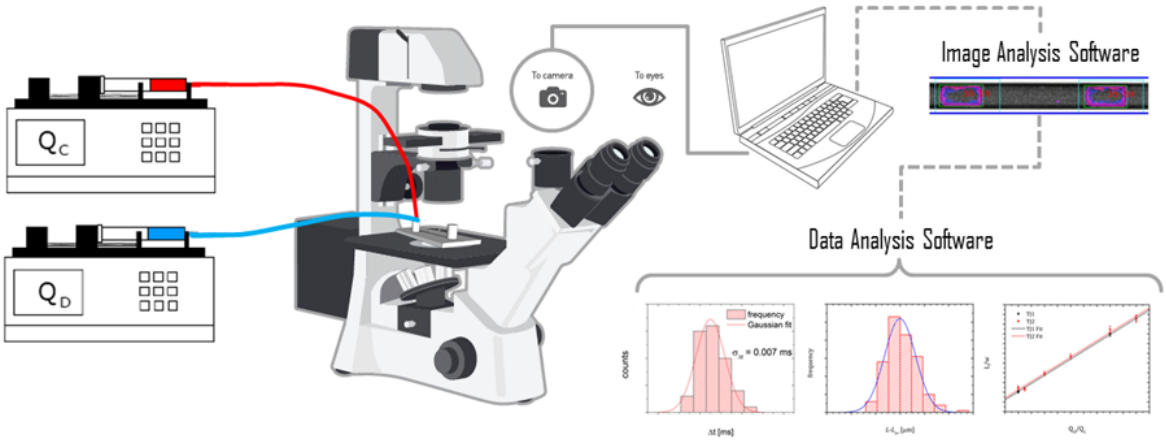

Figure 3.1: *Microfluidic setup from syringhe pumps to Data analysis software.*

Image sequences have been analysed with an image software realized ad hoc by Enrico Chiarello from Lafsi. This software recognized the droplet shape and calculated length, averaged from frames in which droplet appeared, and velocity through fits of position in function of time. A detailed description of this software have been done by the author in [11]. Then output data have been statistically studied with ad hoc realized macros of Root Data Analysis Framework. An example of a typical result with all steps is reported in graphs 3.2.

[1] Hexadecane: $CH_3(CH_2)_{14}CH_3$, CASS number: 544-76-3, Mm = 226.44 g mol^{-1}, viscosity 3cP, density 0.77 $\frac{g}{cm^3}$ @ 25°C.

[2] SPAN®80: $C_{24}H_{44}O_6$, CAS number: 1338-43-8, Mm: 428.62 g mol^{-1}

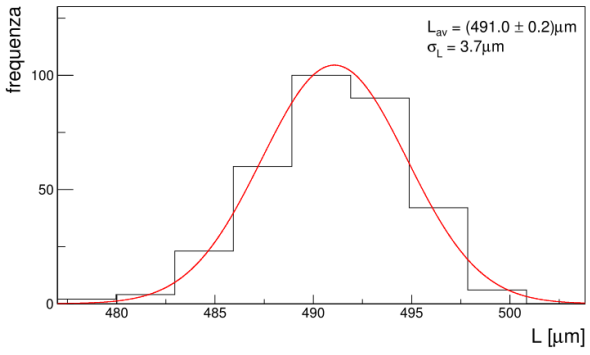

(a) Length of droplet

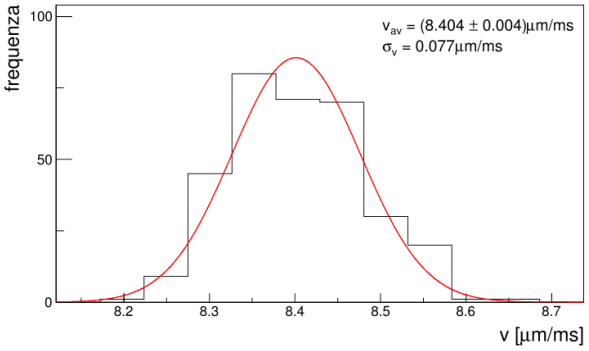

(b) Velocity of droplet

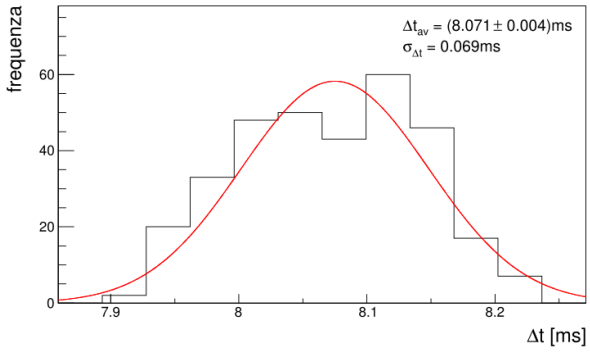

(c) Time between two droplet

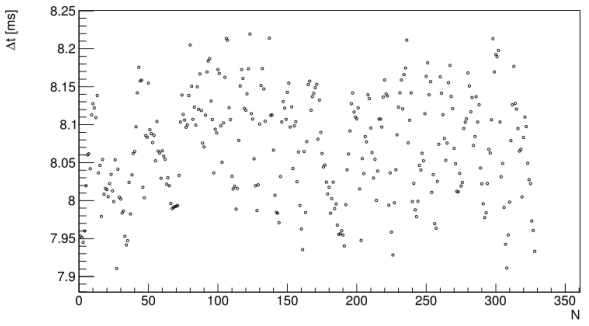

(d) Time between two droplet plotted respect number of first one

Figure 3.2: *Four images refer to a typical microfluidic analysis. This particular one refer to value of* $Q_c = 20$ $\mu L\,min^{-1}$ *and* $Q_d = 30$ $\mu L\,min^{-1}$. *with sample rate of fast camera equal to 860 frame every second. In every graph mean and standard deviation are reported instead of parameters of fit, because Gaussian distribution do not describe a priori the real distribution.*

The distributions of droplet lengths and velocities are reported and were fitted with Gaussian function. Other graphs are reported: time duration of droplets in function of their number (in order to see if there are external systematical fluctuations, for instance due to pumps).
As reported in [11] Standard Deviations [3] of the droplet producer engraved in lithium niobate is around 3% depending on fluxes. This value is surprising compared with standard values in microfluidics.
The complete study with a Microfluidic characterization of these droplet producer integrated in $LiNbO_3$ is already presented in literature by Montevecchi, Bettella and Zamboni in [11, 30, 34], with the same methods of analysis used in this work. For these reasons the performance analysis of Microfluidic droplets is not completely reported in this thesis. Moreover the aims of this work was to demonstrate the feasibility of coupling an integrated MZI to a Microfluidic droplet stage, without deeply studying and characterizing the microfluidic stage. Nevertheless microfluidic measurements used for comparisons between optical results with microfluidics ones, are reported when needed and follow same procedure here and in [11], where it is described in detail.

3.2 Optical setup and characterization

The optical set up used for this work allows to couple a 632,8nm light with both straight waveguides and MZI waveguides. The scheme described in this section have been designed to measure the output of guides and also provide microfluidic integration for optofluidic measurements. The intensity and form of the transmitted beam can be measured and optical losses estimated.

3.2.1 Near field technique

The near field technique is based on the optical coupling of light with the waveguide and detecting the transmitted beam exiting from the waveguide(output). This detection technique is necessary in order to well resolve from background the waveguide output, which has the dimension of the same wavelength used. The optical line is sketched in 3.3. From right to left, stages are:

- **Red Laser**: laser source of $He-Ne$ at 632.8nm with nominal power of 4mW;

[3] Standard deviation refers to $\sigma = \sqrt{\frac{\sum_{i=1}^{N}(x_i-\mu)^2}{N-1}}$ where μ is mean, x_i is data and N is total number of data.

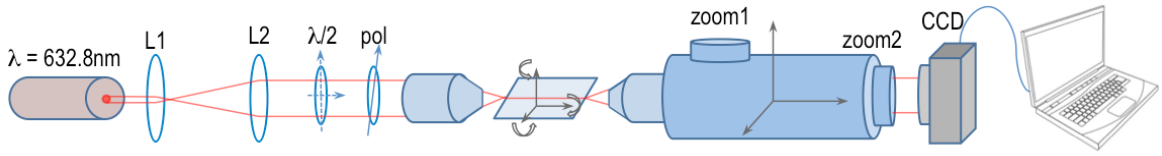

Figure 3.3: *Sketch of set up for measurements of waveguides output form. CCD camera has related software, which illustrated image and give possibility to fit with Gaussian function in both section. CCD connected to the second zoom of x1000 is have been calibrated with standard calibration slide and result is 64.6px/*µm.

- **Confocal lens**: the aim of these lens is to increase laser beam width from 1 to 4mm, which is the entrance pupil diameter of the objective;
- **Polarizer**: half wave plate and polarizer are inserted to excite both TE or TM modes of waveguide. This distinction depends on the direction of electric field respect to the input of the guide.
- **Objective**: to best coupling a 20X objective is used to focus the laser beam on the waveguide entrance.
- **6 degree of freedom stage:** three-dimensional translational and rotational stage to move the sample;
- **Microscope:** microscope in position endowed with an objective 50x with long working distance (1.2cm) and 2 different zoom levels (completely with objective x400, x50), moved by a three dimensional translational and rotational stage;
- **Charge-Coupled Device image sensor (CCD):** LaserCam-HR 1280x1024 camera by Coherent Inc. to record the near field image of the output.

This configuration enables to take images of the output of waveguides in both configurations straigth and MZI. Coherent provides also a dedicated software, which can give images presented in this work and give some statistical analysis like fit of profile.
For measure of intensity, the same set up is used but detector changes. Instead of CCD a silicon based photodiode for visible light is mounted at the end of the Microscope. Photodiode gives a current signal related to the intensity of the incidence light. That signal can be properly measured with different devices depending on the application.
To characterize the optical beam before studying samples, the laser beam was analysed near the focus of the objective: beam profiles have been recorded at different distances with

the camera. Measurements were taken in both directions, then data have been fitted with Gaussian, from which beam width have been derived for every position. Resulting value are reported in graphs 3.4, which fits are function $w(z) = w_0\sqrt{1+\left(\frac{z}{z_R}\right)^2}$. It describe beam width $w(z)$ depending on distance z from focus, w_0 is the waist of Gaussian beam and z_R is the Rayleigh range at which $w = w_0\sqrt{2}$. These last two are used as free parameters for the fits, which had as results: $w_0 = 11.3 \pm 0.6$µm, $z_R = 65.5 \pm 4$ µm and $NA = \frac{w_0}{2z_R} = 0.09 \pm 0.01$.

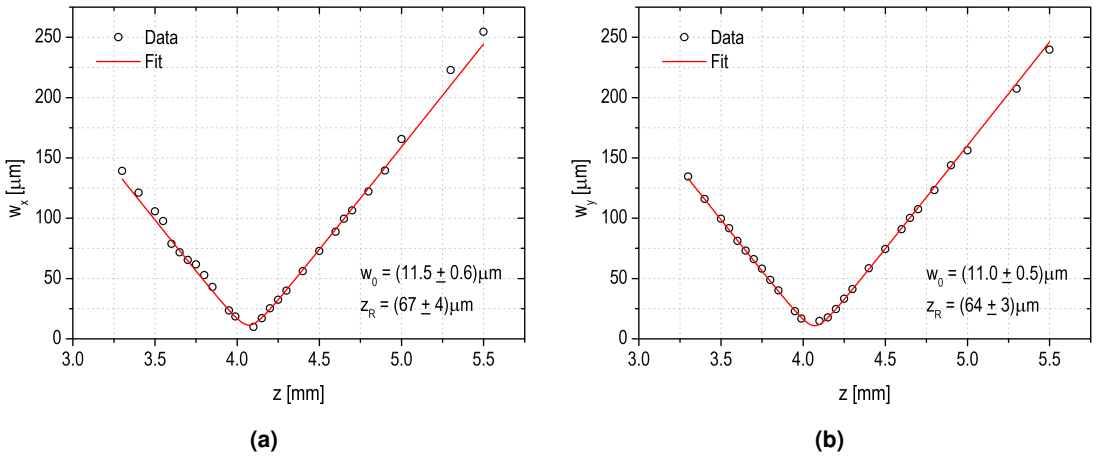

Figure 3.4: *Characterization of the red Gaussian beam employed in this work. The width of the beam are represented on the projections in 3.4a on the (z,x) plane and in 3.4b on the (z,y). Both trend are fitted by the function* $w(z) = w_0\sqrt{1+\left(\frac{z}{z_R}\right)^2}$. *In the bottom right angle beam Waist and Rayleigh range are reported. Errors are smaller than the markers.*

3.2.2 Waveguides optical characterization

Straight waveguide loss

Waveguides have been optically characterized with the set-up described earlier. Both straight and MZI waveguides are studied. Firstly form and intensity of light transmitted by a straight waveguides were measured to understand optical loss due to fabrication process. In fact straight guides are realized with same procedures of MZI configuration, same nominal value of width (5 µm) and same cut of crystal (x-cut). Six guides were realized on the same sample and same set of measurements were performed on all of them. An example of image for an output of a straight waveguides taken by the apparatus described before is reported in 3.5.

Losses of the waveguides are characterized respect to the distance of the waveguides itself. For this reason intensities of different guides were measured varying their lengths,

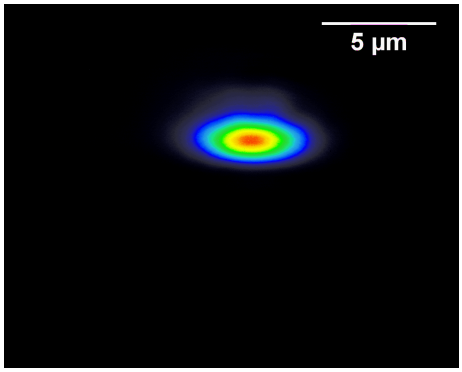

Figure 3.5: *Image of one waveguide used for loss measurements in TE polarization, it have been taken with setup sketched in 3.3 adding proper attenuator to avoid damage on CCD pixel: attenuation value are expressed in Optical density (O.D.), which in this case are 1 O.D.. Calibration have been performed as explained in caption of 3.3.*

in particular the steps followed were: measurements of the transmitted intensities by all 6 guides and then cutting from samples a well-know dimension slice (cut is perpendicular to the direction of waveguides). The intensities for the six guides were measured for seven different lengths[4]. In figure 3.6 graph of guide number 6 is reported as example.

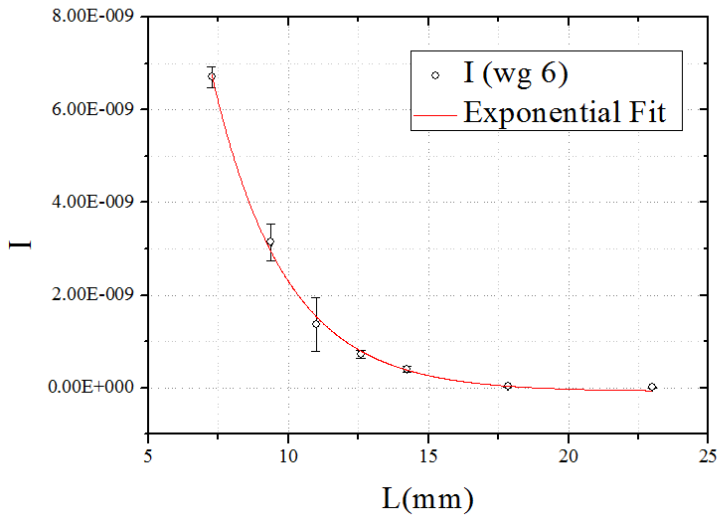

Figure 3.6: *Intensity [Arbitrary Units (A.U.)] in function of the length*[mm] *for the sixth waveguide. Fits are realized with Origin analysis data software and it is a weighted fit of the function* $I = y_0 + I_0 e^{-\alpha(L-L_0)}$ *where free parameter are* y_0, L_0 *and* α.

To estimate error during alignment process at every length first guide was measured ten

[4]Measurements were taken by Dr. Anna Zaltron and Rita Scolaro in Department of Physics in Università degli Studi di Padova

different times, each one after realignment of the sample. From this ten measurements for each length of the sample Standard deviation[5] was calculated in % referring to the mean. This value in % was than considered as the error committed during alignment procedure and was referred to the other 5 guides. Finally this data was fitted with $I = y_0 + I_0 e^{-\alpha(L-L_0)}$, which is the standard formula for transmitted intensity I, where I is the laser beam intensity, α is the attenuation coefficient, L is the length of the guide, y_0 and L_0 are fitting parameters and both resulted compatible with zero. Results of the analysis are reported in 3.1. The attenuation coefficient is usually reported in logarithmic scale $\alpha \overrightarrow{(} logscale) log_{10}(e^{-\alpha})$.

Number of Waveguide	α[dB cm^{-1}]	**Error of** α [dB cm^{-1}]
1	11	3
2	3	2
3	8	2
4	4	3
5	4	3
6	16	1

Table 3.1: *Results from fits of attenuation coefficient for 6 different guides.*

In literature there are only few results about attenuation coefficients for Ti-in-diffusion in lithium niobate for wavelength of 632.8 nm. One of this is [71], where authors reports a value of 2 dB cm^{-1} with prism coupling, which guarantees better intensity.

MZI optical characterization

After measurements of waveguides loss, MZI are optical characterized: the near field measurements of output of transmitted light are taken in the same way of the straight configuration, and same measurements of intensity have been done for Y-branches to understand how light and intensity are split into two arms. First of all images of all possible situation for MZI are taken. The images reported in figure 3.7. Furthermore in every case MZIs present a comparable shape and intensity with other straight waveguides. In this way the comparison between straight waveguide and MZI confirm quality of design of MZI in term of low-loss.

However the quality of these images, observation of MZI highlighted that multiple modes were sustained in waveguides in case of y-propagation. In figures 3.8 are reported first order

[5]Standard deviation refers to $\sigma = \sqrt{\frac{\sum_{i=1}^{N}(x_i-\mu)^2}{N-1}}$ where μ is mean, x_i is data and N is total number of data.

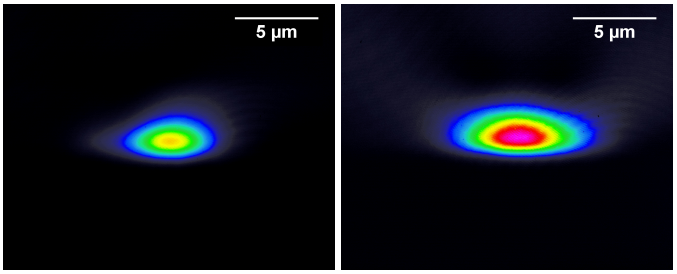

(a) TE, y-propagating, O.D. = 2.4**(b)** TM, y-propagating, O.D. = 1.4

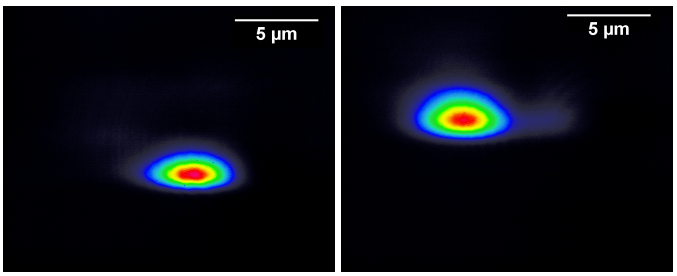

(c) TE, z-propagating, O.D. = 0.4**(d)** TM, z-propagating, O.D. = 0.4

Figure 3.7: *Images of MZI output forms before engraving channels: TE and TM refers to the polarization of the beam respect to waveguide. All images have been taken with setup sketched in 3.3 adding proper attenuator to avoid damage on CCD pixel: attenuation value are expressed in Optical density (O.D.). Calibration have been performed as explained in caption of 3.3. All images are upside down: lithium niobate substrate is in the top half of the pictures.*

mode of the same y-propagating MZI of 3.7. As described in section 2.3 in the fabrication process nominal width are not strictly respected.

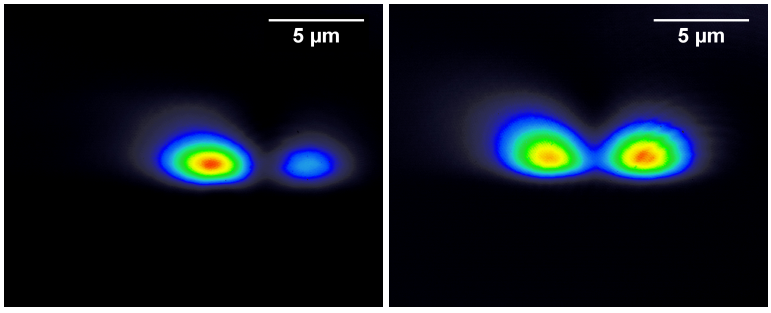

(a) TE, y-propagating, O.D. = 2 **(b)** TM, y-propagating, O.D. =1.4

Figure 3.8: *Images of MZI output forms of first order mode before engraving channels. Both correspond to the same y-propagating MZI of 3.7. All images have been taken with setup sketched in 3.3 adding proper attenuator to avoid damage on CCD pixels: attenuation value are expressed in Optical density (O.D.). Calibration have been performed as explained in caption of 3.3. All images are upside down: lithium niobate substrate is in the top half of the pictures.*

In fact before diffusion stripes width is about 6 µm. The final waveguide width is wider than this values, this is due to the lateral diffusion of the titanium along the direction parallel to the surface and perpendicular to the stripe. This final width probably is the cause of the presence of sustaining by MZI guides of this additional mode. In order to find a solution for this problem, more investigation about this topic have been done. It was realized straight waveguide with 3µm of width and studying their modes. This width have been selected because can provide both good photolitography process and avoid this problem of multi-mode. Same fabrication procedure have been followed to others waveguide of this thesis. Consequently 3µm is demonstrated in figures 3.9 on the next page optimal value of width of waveguide to avoid first mode, and guarantees mono mode guide.

The applications of this width to the MZI configuration is not straightforward, because complication can appear from lift-off. In any case this topic needs more deeply studies to find optimal width, which guarantees best intensity transmission and fit perfectly with MZI configuration.

Checking of 50-50 splitting

The previous characterization (3.7) makes easy to understand that MZI guides light, but there is no evidence about how light is split into two arms. To verify the correct working way,

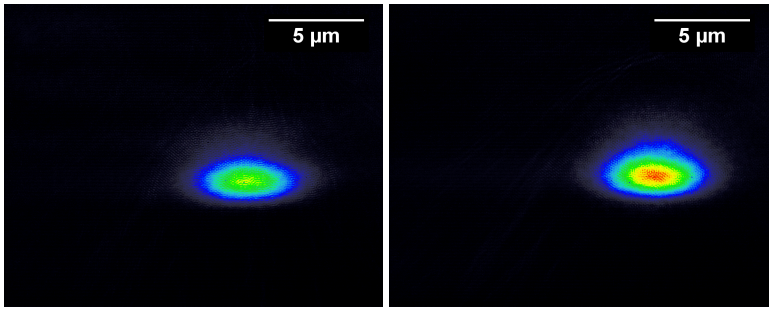

(a) TE, y-propagating **(b)** TM, y-propagating

Figure 3.9: *Images of waveguides of* 3µm *of first mode. All images have been taken with setup sketched in 3.3 without attenuation. All images are upside down: lithium niobate substrate is in the top half of the pictures.*

both arms have to be analysed singularly. For this reason instead of the entire MZI only Y-junction have been realized. Same design and fabrication process of MZIs have been followed. The coupling between the laser beam and the single arm of Y provides transmission of light in both arms and 2 output as expected. Images of both output arms have to be recorded and analysed (figure 3.10). These pictures are useful also to check performances of Y-junction itself, and if really works as power splitter as theoretical expected in 2.2. In fact from theoretical point of view the Ys designed have to split intensity approximately in 50-50%. Figures 3.10 show how both arms present similar behaviour changing polarization. These images presents another feature of MZI arm. Both output arm show sustaining multi-mode, their intensity distribution in fact does not present typical symmetric Gaussian shape of zero-order mode. They acts similarly to a straight waveguide in last section after Y-branch. This evidence is another issue, which supports the hypothesis about multiple modes sustained by a 5µm waveguide. However more simulations and tests have to be done in the next future to clarify the question as mentioned before.

Images 3.10 of two arms transmitted beams clearly denote similar intensity of arms. Further quantitative analysis was realized. For this studies instead of CCD camera, it has been used a Photodiode detector coupled with lock-in amplifier, which cut noise from signal and amplify it. Results of mean processing over 2 minute with relative standard deviation is reported in table 3.2 in arbitrary units.

Considering that every measure needs recoupling and in general moving samples can induce difference between arms with a good level of compatibility. In fact loss cannot be the same in two branches. However this measure confirms similarity of two.

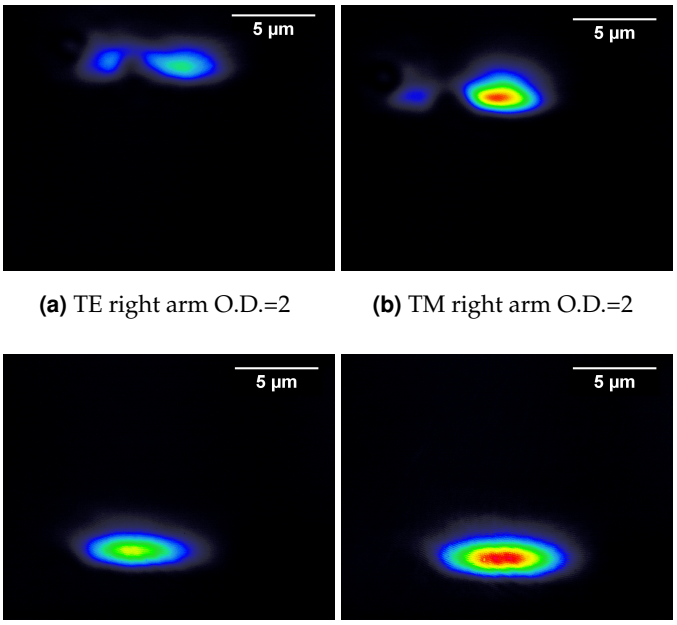

(a) TE right arm O.D.=2 **(b)** TM right arm O.D.=2

(c) TE left arm O.D.=1.2 **(d)** TM left arm O.D.=0.6

Figure 3.10: *Images of Y-branches outputs shape for a y-propagating sample, denotation right and left is from viewing sample on top of surface, where guides are diffused, and seeing from output to input. TE and TM refers to the polarization of the beam respect to waveguide. All images have been taken with setup sketched in 3.3 adding proper attenuator to avoid damage on CCD pixels: attenuation value are expressed in Optical density (O.D.). Calibration have been performed as explained in caption of 3.3. All images are upside down: lithium niobate substrate is in the top half of the pictures.*

arm	**TE**[10^{-9} a.u.]	**Standard Deviation**[10^{-11}a.u.]	**TM** [10^{-8}a.u.]	**Standard Deviation**[10^{-11}a.u.]
right	5.91	1	1.802	4
left	2.54	1	1.976	6

Table 3.2: *Values of average over 2 minute of intensity of both arms, denotation right and left is from viewing sample on top of surface, where guides are diffused, and seeing from output to input. Set up for this measurement diversifies from one in fig. 3.3 for detector: instead of CCD a Photodiode is used coupled with lock-in amplifier and chopper for trigger.*

CHAPTER 4

Optofluidic coupling

The optofluidics circuit performances were characterized by a step by step protocol: each waveguide was characterised when illuminating the microfluidic channel to verify the effect of the presence of channel, first with flowing of fluids, then with flowing of droplets. First measurements of waveguide crossed by microchannel are presented in 4.1. Optical signal from interaction between droplets and light was than interpreted thanks to a simulation in section 4.2, in order to understand how to associate droplet passage to the signal changes. All these characterizations allow for evaluating the sensing capabilities of a single waveguide configuration and understand how interact light from waveguide and flowing droplet. Finally first tests on MZI configuration was exploited in section 4.3.

4.1 Analysis of waveguides crossed by channels

First tests on the optofluidic chip were directed to verify to the coupling and interaction between the two stage. In this work microchannels engraved on $LiNbO_3$ substrate can damage optical waveguides already diffused on chip. Furthermore crossing microchannels modify intrinsically the behaviour of guides. Light path in guide is cut off from channels, so light have to be recollected from outer guide on the lateral surface of channels. In figure 4.1 is presented a sketch of the guide on the top of $LiNbO_3$ chip, crossed by the microfluidic droplet channel. Tests on the working behaviour in this condition for guides are necessary.

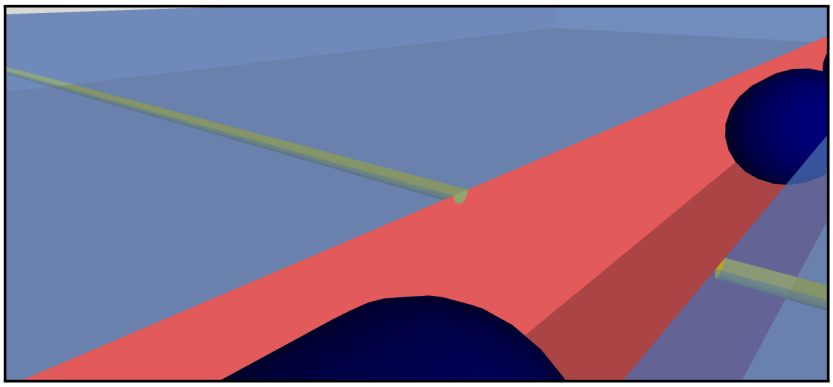

Figure 4.1: *Sketch of the guide on the top of $LiNbO_3$ chip, crossed by the microfluidic droplet channel. Blue substarte represents $LiNbO_3$ substrate, where Ti waveguide are diffused (yellow) and crossed by microchannel (red). On top of the substrate is not drew glass cover for make clearer the scheme.*

In section 3.2 MZIs were already optically investigated in intensity distribution, while in this one MZIs have to be analysed also when arms are crossed with channels. Since arms of interferometers behave as a straight waveguide in the parallel section, simple straight waveguides have been used for these tests, thank to their higher intensity. Same conclusions can be derived from the results on those guides for the single a arm of MZI.
Three different images of the light propagating into the waveguides and illuminating the microchannel that cross it, have been taken with CCD camera in the set up described in 3.2 varying the fluids fluxing in the channels: air, water and hexadecane. Obviously not all the intensity coming from first half of waveguide, that acts as input waveguide, is collected by the second half after the channels due to angular dispersion. When the channel is filled by air only 38% of intensity without channels is recorded in the same configuration. Filling channels with other fluids change Fresnel coefficient of refraction and consequently Angular dispersion. With hexadecane the transmitted intensity rises up signal to 76% respect to case of air, while water increase signal to 46%. Images are reported in figure 4.2.

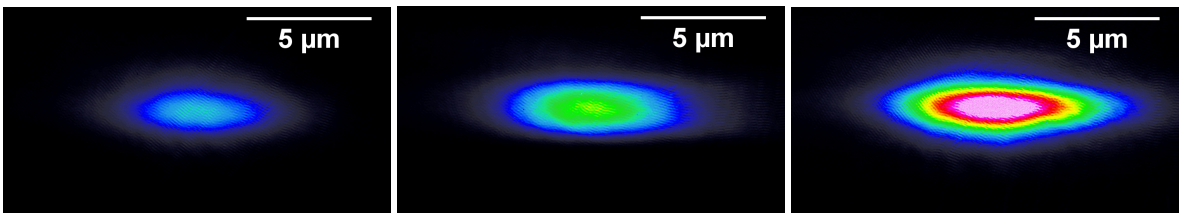

(a) Air $\frac{I}{I_0} = 38\%$ **(b)** Water $\frac{I}{I_0} = 46\%$ **(c)** Hexadecane $\frac{I}{I_0} = 76\%$

Figure 4.2: *Example of a near field image of a y-propagating waveguide coupled to a 200* µm *wide microfluidic channel: from the right channel is filled with air, water and hexadecane.*

Similar tests have been made to verify influence of proximity of glass cover to the output and input of waveguides. Images have been recorded before and after application of the cover. Glass cover does not seem to influence the signal, waveguides preserve in fact both shape and intensity distribution. However another critical point derives from the location of guides respect on channels.
Droplet curvature near top of channel can complicate interpretation of optical signal (see section 4.2). Different way to realize waveguide in the centre of channels were considered in this work, considering that the waveguide fabrication method via diffusion limits realization on a free surface of the crystal:

- **Sandwiching of two samples**: one hypothesis is to fabricate half channel on two different samples and on one of them also waveguide circuit. Then through alignment machine two samples have to close one on the other, paying attention on channels alignment.
- **layer of polymeric material**: before engraving of the microfluidics channels on chip. Thin layer of the polymeric material like PDMS or similar can be deposited on the surface, and than both in this material and $LiNbO_3$ can be engraved channels.
- **Sputtering**: another idea consisted in the sputtering of oxide on sample surface. First waveguides circuit desired have to be realized, then a layer of oxide with thickness similar to the height of channels, have to be sputtered on surface, before microchannels engraving. In this way microchannels depth extends inside the oxide and half in $LiNbO_3$, leaving guides in the centre.

First of three methods is not feasible due to unavailability of a precision aligning machine. Second one is unattainable due to the poor stiffness of polymeric material. Some tests with NOA68 have been done but, near the diced area, the material results crumbled, making the sealing liquidtight procedure impossible. Also for the third one some tests with Zirconium Oxide have been done, but demonstrated to be unsuccessful. For a layer about ten of µm systematic study and more time is needed, and went beyond the aim of this thesis. Further research about this topic will be followed in the future.
Nevertheless the failure, preliminary analysis on guide in the centre of the channels have been done using chips where waveguides are situated in the centre of the height of microchannels thanks to the NOA68 layer. Unclosed channels on this chip are filled with the same three fluids used for top situated guide to compare the behaviour of the two. As expected same results are obtained for centered guides.

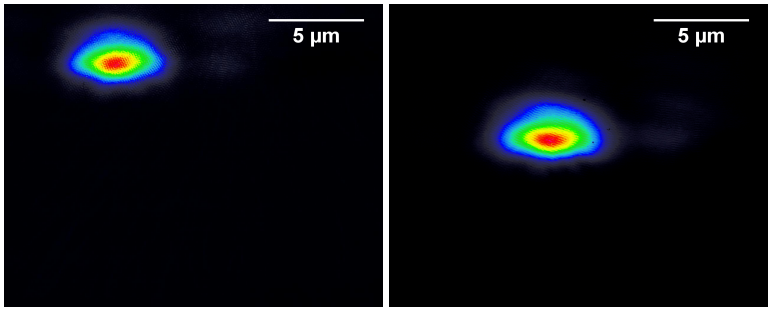

(a) Air, TM, O.D.=0 **(b)** Hexadecane, TM, O.D.=0.6

Figure 4.3: *Images of waveguides in centre of the channel filled respectively with air and hexadecane. Both cases present similar shape and intensity distribution respect to the top ones.*

4.2 First Optofludic Droplet Result

In this section it is presented the first optofluidic signal of a droplet provided by optofluidic coupling between Droplet generator and waveguides in $LiNbO_3$. As expected from measurements of the section before, optical signal results lower when water (or aqueous) droplets flowing in front of a waveguide than continuous phase. In this way supposed signal is a squared signal, where higher plateaux corresponds to hexadecane, while others to the droplet. Instead there are not the same expectation about menisci passage. Curvature of droplets at the interface between dispersed and continuous phase can influence in various way the signal.

For understanding the signal and analysing it, additional test have been implemented: straight waveguide were realized and coupled with Microfluidic stage. Droplets of a single continuous phase were produced by the Cross-junction in T-junction configuration, then analysed with a single straight waveguide. Same set-up for optical characterization of guides have been used, but different detector: instead of the CCD camera, a Photodiode with in cascade a transimpedance amplifier (same photodiode used in section 3.2 on page 52 for measurments of intensity of MZI arms). This detector measures the intensity giving as output a current signal proportional to it, transimpedance amplifier amplifies and transforms it into difference of potential signal.

In addition to the optical set up, the same syringe pump for Microfluidic characterization 3.1 on page 49 are used to set flows. Furthermore an Analog to Digital Fast Card NI 6023E is used to record voltage signal derived from transimpedance amplifier. This card can guarantee a measurements sensitivity of voltage reading of 0.0023 mV and maximum sample rate of 200 $\frac{KS}{s}$.

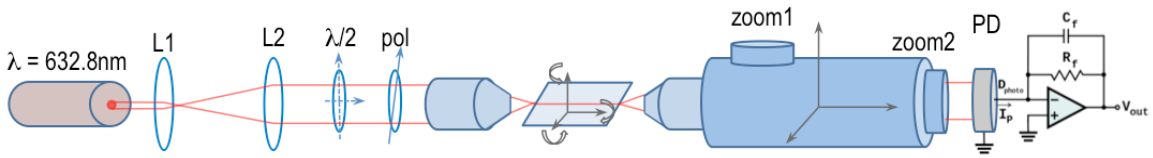

Figure 4.4: *Sketch of set up for measurements of waveguides intensity.*

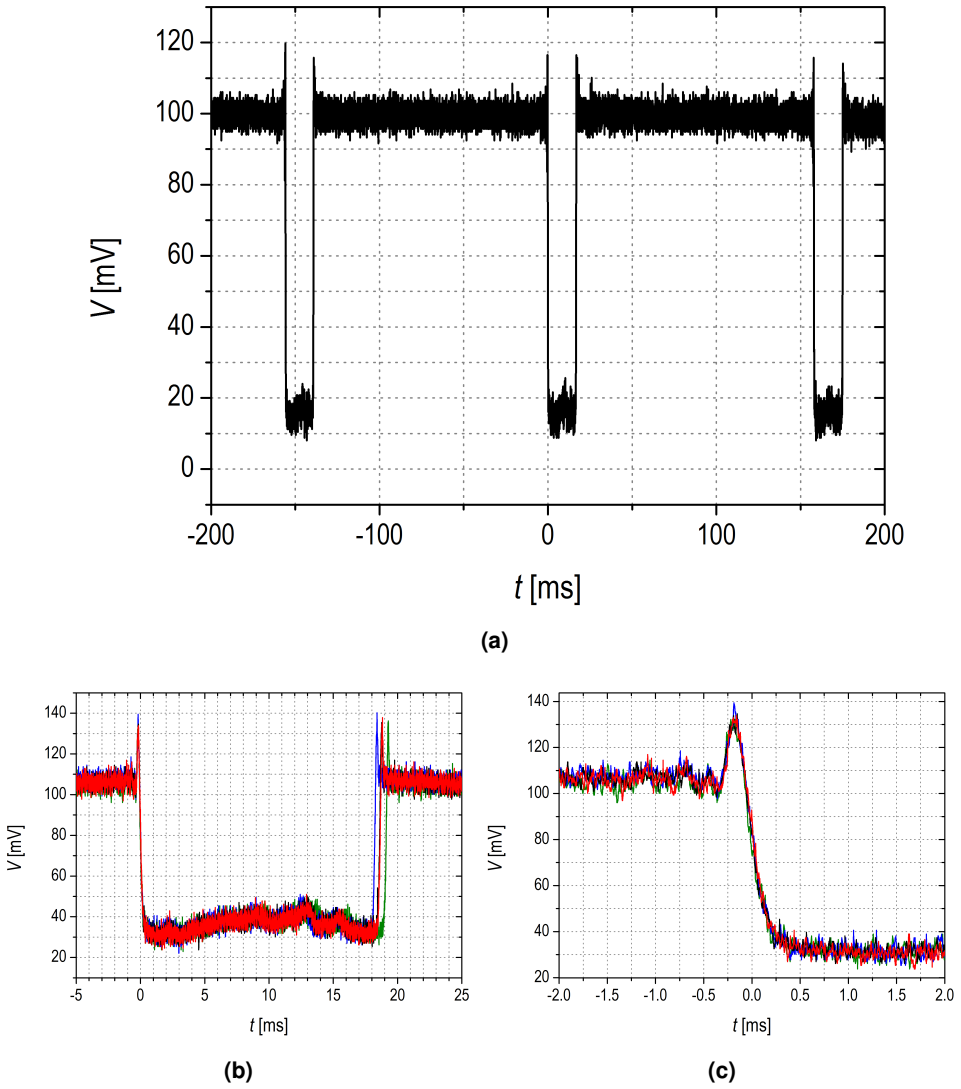

Figure 4.5: *First results of voltage droplet signal, this images were realized by Bettella in [30], using Oscilloscope instead Fast Card. 4.5a Three subsequent droplets; 4.5b superposition of the signal from four different single droplets as triggered by the oscilloscope on the negative slope; 4.5c insight of the previous image showing the high repeatability of the signal shape.*

First measurements were performed by of straight waveguide as said before: droplet

produced from T-junction (cross-junction with one inlet closed) are in Milli-Q water while dispersed phase in hexadecane. As highlighted from first measurements 4.5 when droplet flow in front of a output of waveguide, changes drastically when water fill channel. Straight waveguide were used for this application are z-propagating, but only because of intensity is higher for z-propagating. Both polarizations were tested and same typology of signal is given, only the intensity changes.

Example of the signal of flowing droplets are figured in 4.5. As shown in 4.5c the signal exhibits extremely high reproducibility in shape, in particular the first part of droplet where unexpected increase are located. As expected signal falls when droplet flows, so length of holes depends on length of the droplet, distribution strictly depends on quality of droplet generator, precision of flows and the temperature (physical properties of fluids like viscosity change with temperature). However the shape of droplet signal shows high reproducibility: every droplet present same parts: increase before step of water, same oscillation on the water signal, than symmetry step to the first half.

The experimental configuration used helps not only in understanding coupling between with droplet and waveguides, but has an important application as droplet counter. This feature is very important in droplets microfluidic, not only from simply counter point of view but this configuration can easily work as triggering stage for other application. Simply acquisition program to count droplet have been programmed through Root data analysis software.

Once the signal was acquired, investigation of shape was indispensable to associate exactly flowing droplet parts to the signal. In particular shape and spike before fall of droplet is quite interesting for its reproducibility and its unknown origin. To understand better the spike some simple ray simulation with C++ have been written by the author. Instead of the more used finite elements simulation simpler ray light simulation have been used because of the dimension of the system. In fact the dimension of channel respect to the guides makes simulation of electric field through Maxwell's equation too expensive in term of CPU cost. In this way rays optics approach is simpler but more feasible. For the same reason mentioned before, another approximation is consideration of leaving rays only interacting with menisci interface in the same section. For simplicity, the growing of menisci interface during the droplet flow has been evaluated and the section of menisci is considered spherical until top part of droplet reach top of the channel. Rays collected from more than three refractions and from the top of the channel, are considered negligible. In figure 4.6 is sketched all this approximations for visualize better the simulation.

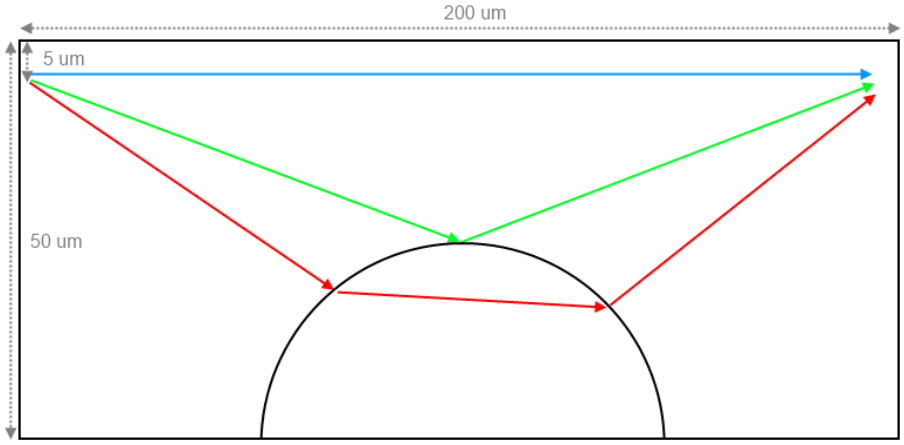

Figure 4.6: *Sketch of the top half of microfluidic channel seen from orthogonal section. Flowing droplet profile is considered spherical for simplicity. Blue lines represent directed rays collected from other side waveguide, Reds double refracted rays and greens reflected. Sizes of channels are the same of first test done: height: 200* µm *width: 100* µm.

The height of guide is divided in H sources of rays. From each of this source N rays are simulated at different angle: from 45°, which is the maximum angle of exiting ray to interact with menisci to be reflected in the top half of the channel, to maximum angle for be recollected without interaction with droplet from waveguide on other channel side. Time of menisci flow is discretized in M intervals. For each rays generated, the simulation counts how many of them are then collected in three cases: if they enter directly, after the reflection on droplet or double refraction inside droplet. This three counter of rays are then normalized to the total amount of rays generated i.e. $N \cdot H$. Totally the simulation gives for M times collected rays in three cases mentioned before normalized to the amount of generated rays. Results for menisci of water immersed in hexadecane, M=1000, N=10000, H=100 and channel 200x100µm are reported in figure 4.7.

Figure 4.7 shows also decreasing of the signal, this is calculated in analogous way of other points, apart from the fact that the droplet fill completely the channel darken direct and reflected rays. Direct and reflected from this point are zero, while number of double refracted keeps growing. Approximation of droplets grow is that it keep spherical shape during growth with radius changing from 50 to 100 µm. So as shown in figure 4.7 the signal fall prediction is when radius of curvature of the droplet reach a value equal to 1.1 time respect to the height of the channel.
Despite the simplicity of the simulation, it predicts well the growth of the signal until a

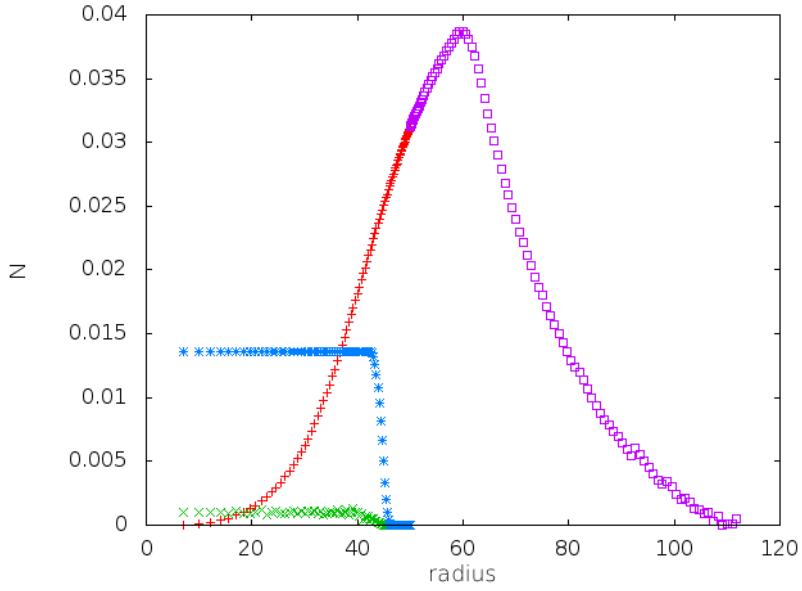

Figure 4.7: *Results of the simulation for number of rays N, collected from guides on the other side of the channel, normalized to the total rays generated. Colors correspond to 4.6: blue rays are direct, reds are double refracted, greens are reflected and violets are double refracted when the droplet is blowing up itselfs with radius higher than half height of the channel. Data reported refer to the change of radius of curvature of the droplet.*

maximum then fall during menisci flows, fact which has been verified. Furthermore it predicts that maximum is not when the radius of droplet menisci is higher than half of height of the channel, exactly when its about 20% higher. However this simulation does not aim to describe in detail menisci signal, but at least confirms the expectation about the grow of the signal during menisci flows. As it can be seen from figure 4.7 simulation well explain this behaviour.

This simulation is only the first step of a more detailed and precise study about optofluidic interaction between flowing droplet and waveguides, which is a wide and complicate field of research. In the next future lots of already developed strategy to investigate this arguments will be followed.

4.3 Results and analysis of MZI coupled with droplet Microfluidic

First measurements of the droplet signal from Mach-Zehnder configuration are here presented and discussed. Different working regimes are expected varying ratio between lengths of the system: droplet one, length of continuous phase between two droplets and the distance between arms of MZI. In the same way of single waveguide exposed in section

3.2 different fluids in front of a waveguide implies different intensities. In the case of MZI possible configuration is more complicate due to the presence of two waveguides interacting with microchannels. Indeed a different intensity from each arm of MZI is transmitted varying the fluids in front of it. For this reason, different ratios between droplets, continuous phases length and arms distance generate several typology of signal. For simplicity different possible situation are schematized with: *CC* when both arms are covered with continuous phase, *DC* when only in front of first arm (first encountered following flows direction) there is continuous phase, *DD* when droplet filled all channel at least from first to second arms and last one *CD* is simply vice versa of *DC*. In 4.8 all four regimes expected from author are illustrated.

The **first one** 4.8a is simplest and it is when droplet length and length of continuous phase between droplets are longer than distance between arms $L_{continuous} > 2W$ and $L_{dispersed} > 2W$. Expected signal is quite easy to predict: droplet can cover both or each one singularly the arms, and all situations are presented in a precise sequence: *CC* no droplet, *DC* droplet cover first arm, *DD* droplet cover both of them, *CD* droplet cover only second one and again *CC* no droplet (C refers to continuous phase, while D to dispersed one. First letters refer to the first arm encountered by droplet, and second to the other one).

The **second one** 4.8b is verified when droplet length is smaller than distance of arms, but continuous phase keeps to be longer $L_{continuous} < 2W$ and $L_{dispersed} > 2W$. In this case expected signal is similar with difference that this time droplet cover one guide at one time. Situation called before *DD* is not observed in this regime and the sequence in this case is: *CC* no droplet, *DC* droplet cover first arm, *CC* droplet is in-between arm but not in front any of the two, *CD* droplet flow in front of second arm and again *CC* no droplet.

The **third one** 4.8c is complementary to the second one: droplets are longer than arm distance, while distances between droplets are smaller $L_{continuous} > 2W$ and $L_{dispersed} < 2W$. *CC* is the situation unattainable in this regime, for this reason is the regime with lowest signal. In this case the sequence is more difficult to read because, instead of following the flow of one single droplet, it follows one continuous phase passage: *DD* one single droplet cover both arms, *CD* continuous phase flows in front first arm, *DD* continuous phase is in-between arm, but does not cover any of the two arms and two different droplet cover arms, *DC* continuous phase flow in front of second arm and again *DD* one droplet cover both arms.

The **fourth one** 4.8d is the last possible situation: both length of droplet and continuous phase are smaller than arm distance $L_{continuous} < 2W$ and $L_{dispersed} < 2W$. In this regime the device cannot extrapolate information from the output signal. In fact there are not any possible ways

to know how many droplets are between two arms of interferometer in each instant, without using another sensing way.

In order to identify and study all regimes particular solution for the measurements have been adopted. Same setup of last section for droplet sensing have been used, but with the device on which MZI configuration are realized. Cross junction of the device is used as a T-junction to produce signal of single continuous phase droplets. To be sure that signal of both arms can be recognizable from background, instead of other applications air droplets in hexadecane were produced. In fact this configuration guarantees higher difference in optical signal between droplet and continuous phase. On the hand air droplets do not show same regular trend of water droplets. Since air is a compressible fluid, the pressure in channel cannot be stable, specially in case of pumps with flows control instead pressure, which were not available. Nevertheless the spread in air droplet length provides all possible working regimes, which are perfect for testing device.

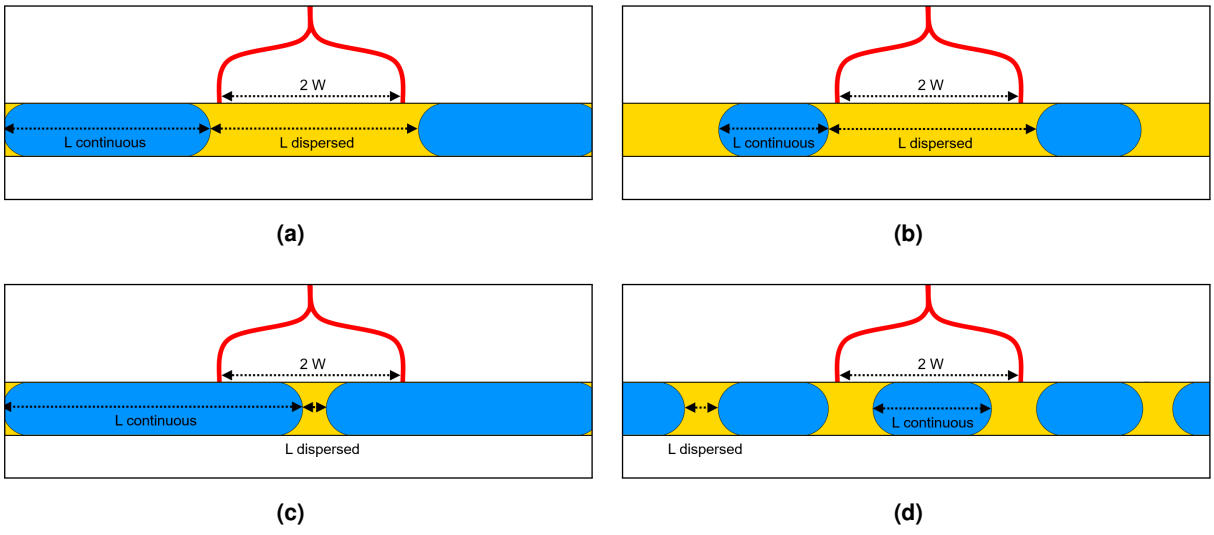

Figure 4.8: *Sketches of all possible working regimes of the device.*

One typical output signal for each regime is reported in 4.9. As shown in 4.9 the device can well distinguish the regimes, also the situations *DC* and *CD* are well-defined through the average voltage levels thanks to the difference in intensity in two arms (In figure 4.9 green square represent part of the signal where first arm covered from droplet *DC*, while blue when second arms is covered *CD*.). This asymmetry in intensity of two arms can be verified and calibrated before acquisition, focusing on output of the guide in the channels through high working distance (more than half of the sample) objective used (see 3.2). This small

asymmetry is fundamental to distinguish *DC* from *CD* and so in record droplet properly. In fact thanks to this expedient the device can retrace any droplets sequence without knowing anything about that, expect from the fourth regime. In this way, avoiding the last regime, every part of the optical signal can properly associated to a situation described before and the story of the droplets flowing can be retraced. Specially velocities and lengths of every droplet can be extracted from the signal.

To obtain and properly analyse signals deriving from the device a Root macros have been used, realized with the collaboration Dr. Giacomo Bettella. Every time that the signal changes significantly program tracks properly all different situation recognizing as element called plateaux. For each plateaux it calculates mean and its error from all voltage values. The resulting averages of all plateaux are graphed in histogram: an example of this one is reported in figure 4.10, as graph shows four distribution is easily observable corresponding to the four situation listed before: *CC*, *DD*, *CD*, *DC*. To considering potential oscillation of all signal that can influence voltage distribution, same histogram are plotted in figure 4.10 to the plateaux averages normalized both to the nearest plateaux referring to *CC*, *DD* respectively. As shows from histograms distributions do not exhibit different width, this fact means that system do not present any oscillation and remaining stable over all the time of acquisition. All four distribution of voltage are then fitted with Gaussian function in order to set proper interval to associate to the one of the situations. Despite the air droplets flowing in the channel present random lengths, device recognizes four well defined and different plateaux. Value of the Gaussian fits in table 4.1 exhibits how well device can distinguish four plateaux. This sensibility to the plateaux means a sensibility to the droplet recognizing process.

From the signal, as mentioned before, it can be derived lengths and velocities of the droplet. In each regimes each droplet is localized between four steps of signal. Knowing the distance between MZI arm $2W$, velocity is calculated as follow: the ratio between $2W$ and the difference in time between step corresponding in the cover by advancing menisci of first MZI, and cover of second arm by the same menisci. Measured velocity, length simply can be calculated as: the ratio between velocity and the difference in time between step corresponding in the cover of first arm by the advancing menisci and by following one. In this way a complete analysis of the droplets characteristics is provided from the device.

The possibility of measuring flowing droplet of unknowing flows make this device as one of the most innovative in field of Optofluidic and more in general in Lab-on-a-Chip

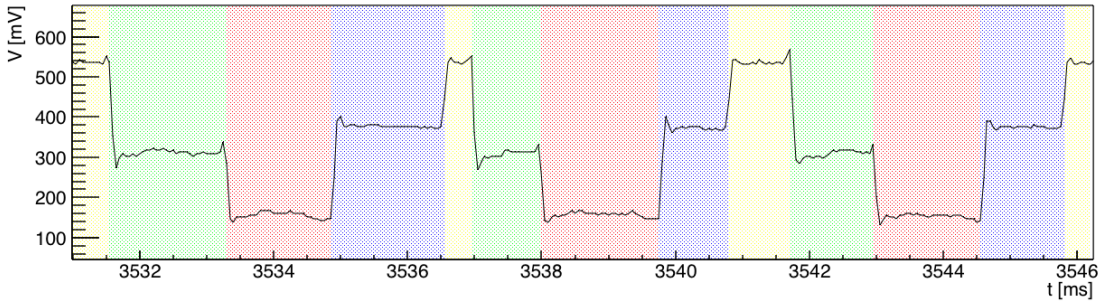

(a) Corresponding signal for 4.8a

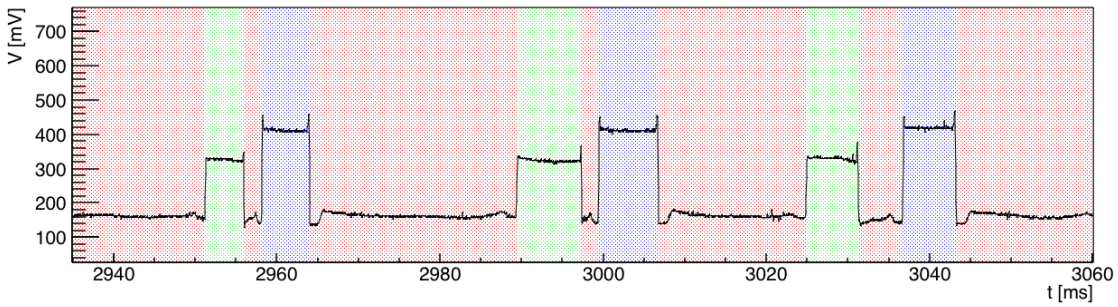

(b) Corresponding signal for 4.8b

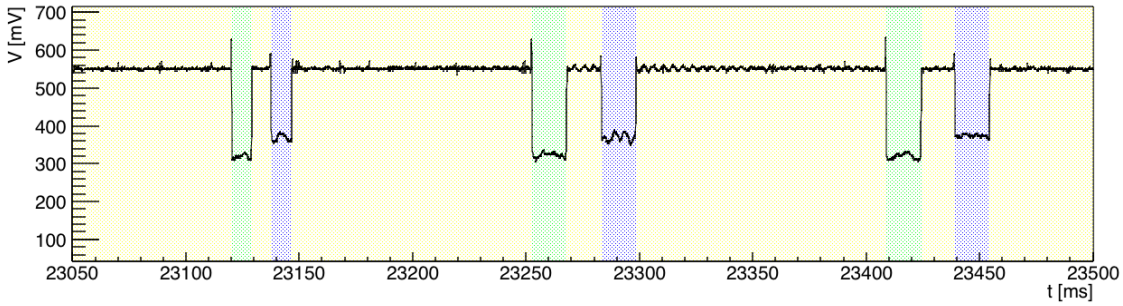

(c) Corresponding signal for 4.8d

Figure 4.9: *Examples for all of 3 possible working regime. All this signal are taken with same setup used for first test with straight waveguides. Sample rate of Fast card was setted to 20000 $\frac{KS}{s}$. Different colors are attributed to different plateaux: yellow corresponds to the situation called CC, green to the DC, blue to the CD and red to the DD.*

	DD	*DC*	*CD*	*CC*
μ	160 ± 0.3	295.8 ± 0.4	362 ± 0.4	504 ± 0.6
σ	6.5 ± 0.3	5.4 ± 0.3	5.4 ± 0.4	4 ± 0.9

Table 4.1: *Results of the Gaussian fits in figure 4.10a. Where μ and σ refer to parameters of Gaussian fit $f(x) = ae^{-\frac{(x-\mu)^2}{2\sigma^2}}$.*

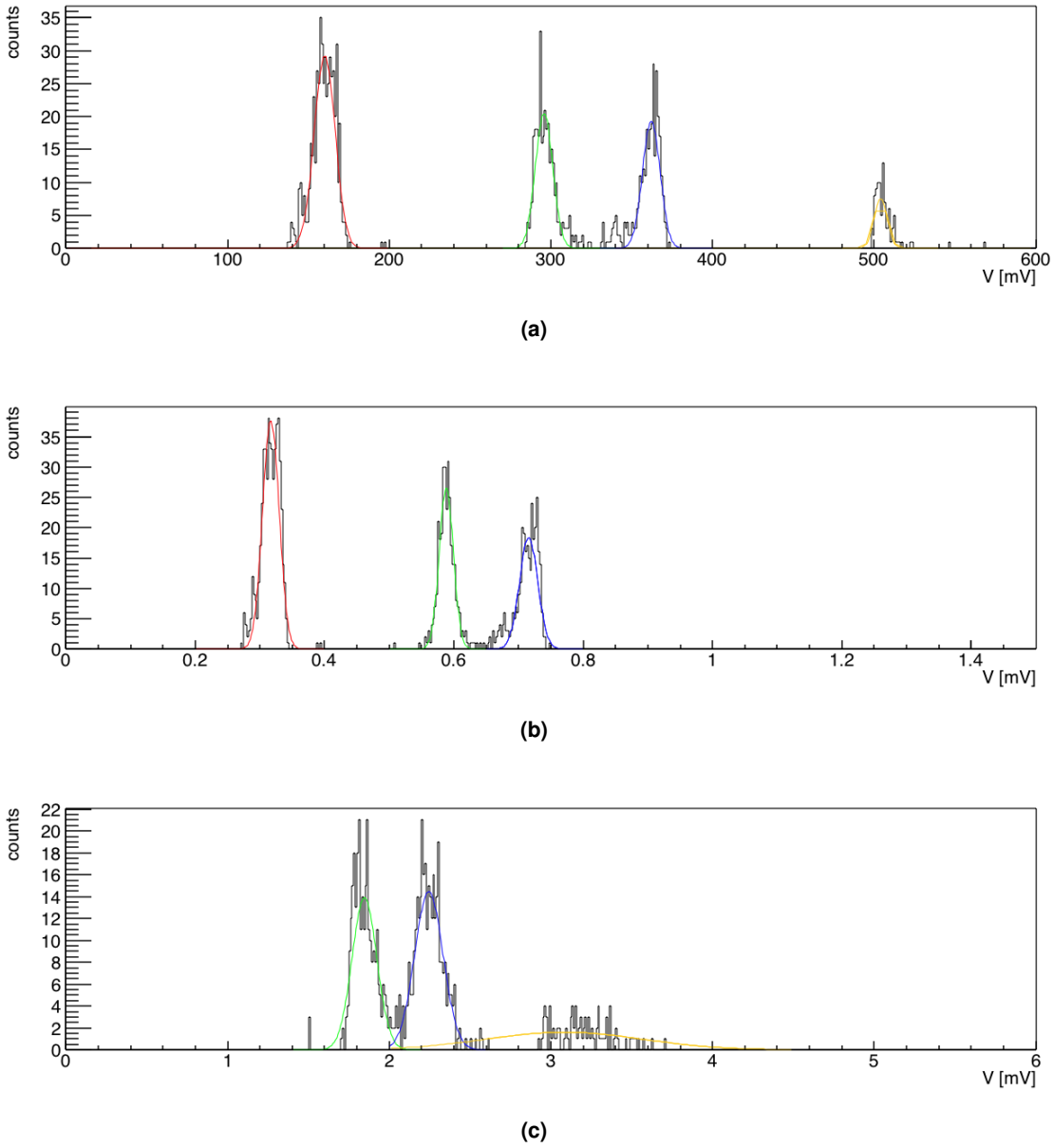

Figure 4.10: *Distributions of the averages of voltage values : top one is simply the distribution of voltage average of all plateaux, in the second one from top all averages are normalized to the nearest higher plateaux (nearest DD) and in the third they are normalized to the nearest lowest deeper (nearest CC). All distributions are fitted with Gaussian function.*

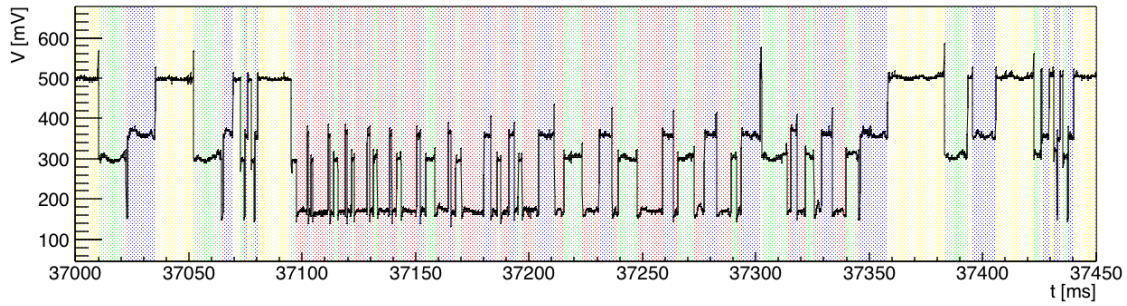

Figure 4.11: *Examples of a signal of a random air droplets.*

application. In literature there are not any reference about the possibility of recognizing and retracing an unknown sequence of droplets with different lengths and velocities. This feature make device extremely interesting, both as precise and autonomous analysis tool and as a feedback to strictly control droplet volume for flow pumps. Indeed voltage signal is most controllable typology of signal, and triggering analogic system can be easily integrated.
This promising results open the possibility to future test on others liquids to check if this distribution can be distinguished even with aqueous fluids. Indeed test have to be done with more regular droplets flows in order to verify the spread of this four distribution. The capability of distinguishing this distribution is the key to recognize droplet and properly associate it to the liquid filling Microchannels.
Next step programmed for the near future are using the Cross-junction with 2 different dispersed phases to index of refraction sensing in the same way of Bettella and Montevecchi [30, 34].

Conclusion

The aims of this thesis were the fabrication, and characterization of an optofluidic device integrated in $LiNbO_3$ substrate for droplet sensing. The device is composed by two stage: Microfluidic and Optical. For both of them a detail description of the fabrication and characterization is given. Firstly Lithium Niobate have been described as a valid alternative of common Optofluidic material, thanks to his multiple properties and opportunities of integration of both integrated microfluidic and optical stages.
The details of the working behaviour of the microfluidic stage have been reported, it consists in Cross-junction. A brief review form literature has been done in order to understand the law, which described droplet produced by this apparatus. The geometry of the microchannels have been already used and described in other few work, but this is first time that 50x50 µm microchannels in Cross-junction configuration is engraved on lithium niobate.
Optical stage consists a Mach-Zehnder Interferometer waveguided for a 632.8 nm wavelenght in $LiNbO_3$, which is usually used for Optical fiber-telecom applications. In this work a completly new employment for droplet sensing have been reported. For these reason, a new design have been studied starting from the state of the art about Mach-Zehnder interferometer. From this study have been derived a low-loss design of interferometer for a specific application in droplet sensing. The final design have been realized through thermal in-diffusion of thin titanium stripes deposited on the surface of the crystal by joint sputtering and photolitography techniques. Profilometry, Atomic force microscopy and optical Microscopy techniques were employed to check the different steps during fabrication.

Each step imprecision of fabrication was improved, in order to find optimal fabrication sequence and precautions to be take during development of the final optical stage. Reached

loss of the waveguides due to fabrication quality is around 3-4 dB cm^{-1} which is in line with others waveguide in lithium niobate for 623.8 nm, this value demonstrated be higher than design loss provided by critical part of the Mach-Zehnder configuration.
Transmitted light of the waveguides used for this work have to be mono mode for the best comprehension of interaction between droplet and light. This constraint push to a characterization of waveguide in intensity distribution to check the mode sustain. Straight waveguide were realized with nominal width of 3 and 5 µm were fabricated, first result sustaining only zero-order mode, while other in TE polarization of the input beam shows also first-order mode. For this study a Near Field setup have been used and deeply described in this thesis. Same setup was used to optical characterization of Mach-Zehnder interferometers. Intensity distributions of output of the Interferometers are reported in both TE and TM polarizations of the input beam for both possible direction of propagations i.e. y and z. However evidence that both arms of interferometers transmit light is given only through fabrication of particular Y-branches and S-bend in order to study how well design split beam in the two arms. Intensity measurements highlights that both arms transmit approximately half of the input light.
Last part of this thesis is reserved to the optofluidic coupling. After integration of both stages on the same chip of $LiNbO_3$ waveguide output were checked again. The recollected light after microchannels do not influence output of waveguide in distribution intensity, excepted for the total intensity which is demonstrated depending on the filling channel fluid. Test are performed with water, air and hexadecane, which are typically used fluids in Microfluidics. The same fluids are used to produce droplets, in particular droplet of water and air are produced in hexadecane. Water droplets are first analysed with straight waveguides integrated in the same chip of Cross-junction. THis device are used for testing the interaction between droplet and light. The optical signal from output of waveguide is collected through silicon photodiode coupled with transimpedance amplifier, in order to obtain voltage signal. The signal of droplet result quite surprising, in particular when flows menisci of droplet: it present spikes right before drop to the value attributed to the water. The spike is attributed to the flows of the menisci through a rays light simulation, which simulates the interaction between flowing menisci and light rays generated from waveguide.
Once understand droplet signal, final device was tested with air droplet to guarantee highest drop of signal during droplet passage. A complete analysis of the signal were realized: four working regimes have been individuated, each one characterized by different sequence between the possible configuration of droplet and two arms. Device have been demonstrated reading random droplet sequence and tracking them. Indeed this first test have been realized

with air droplets, which generate droplet in different regimes, and the device are able to reconstruct all sequence of droplet and characterize their length and velocity, without integration of any other sensing system. The device reaches aims predicted, but also its potential keeps open lots of improvement and testings.

This promising results represents only first step: the potential applications of the device is wide. In next future a better calibration with other fluids will be realized. Then a research on index of refraction sensing through of flowing droplets of two fluids is already programmed. Furthermore lithium niobate integration properties opens multiple innovative challenging Lab-on-a-Chip devices,based on monolithic substrate of this material similar to the one presented in this work.

Bibliography

[1] Emanuel Weber, Dietmar Puchberger-Enengl, and Michael J Vellekoop. In-line characterization of micro-droplets based on partial light reflection at the solid-liquid interface. In *ASME 2012 10th International Conference on Nanochannels, Microchannels, and Minichannels collocated with the ASME 2012 Heat Transfer Summer Conference and the ASME 2012 Fluids Engineering Division Summer Meeting*, pages 589–595. American Society of Mechanical Engineers, 2012. (Cited on page 1)

[2] Martha-Elizabeth Baylor, Benjamin W Cerjan, Charlotte R Pfiefer, Robert W Boyne, Charles L Couch, Neil B Cramer, Christopher N Bowman, and Robert R McLeod. Monolithic integration of optical waveguide and fluidic channel structures in a thiolene/methacrylate photopolymer. *Optical Materials Express*, 2(11):1548–1555, 2012. (Cited on page 1)

[3] Roberto Osellame, Valeria Maselli, Rebeca Martinez Vazquez, Roberta Ramponi, and Giulio Cerullo. Integration of optical waveguides and microfluidic channels both fabricated by femtosecond laser irradiation. *Applied physics letters*, 90(23):231118, 2007. (Cited on page 1)

[4] F Bragheri, P Minzioni, R Martinez Vazquez, N Bellini, P Paie, C Mondello, R Ramponi, I Cristiani, and R Osellame. Optofluidic integrated cell sorter fabricated by femtosecond lasers. *Lab on a Chip*, 12(19):3779–3784, 2012. (Cited on page 1)

[5] Rebeca Martinez Vazquez, Roberto Osellame, Marina Cretich, Marcella Chiari, Chaitanya Dongre, Hugo JWM Hoekstra, Markus Pollnau, Hans van den Vlekkert, Roberta Ramponi, and Giulio Cerullo. Optical sensing in microfluidic lab-on-a-chip by femtosecond-

laser-written waveguides. *Analytical and bioanalytical chemistry*, 393(4):1209–1216, 2009. (Cited on page 1)

[6] Alvaro Casas Bedoya, Christelle Monat, Peter Domachuk, Christian Grillet, and Benjamin J Eggleton. Measuring the dispersive properties of liquids using a microinterferometer. *Applied optics*, 50(16):2408–2412, 2011. (Cited on page 2)

[7] Andrea Crespi, Yu Gu, Bongkot Ngamsom, Hugo J. W. M. Hoekstra, Chaitanya Dongre, Markus Pollnau, Roberta Ramponi, Hans H. van den Vlekkert, Paul Watts, Giulio Cerullo, and Roberto Osellame. Three-dimensional mach-zehnder interferometer in a microfluidic chip for spatially-resolved label-free detection. *Lab Chip*, 10:1167–1173, 2010. (Cited on page 2)

[8] Qing Liu, Xiaoguang Tu, Kyung Woo Kim, Jack Sheng Kee, Yong Shin, Kyungsup Han, Yong-Jin Yoon, Guo-Qiang Lo, and Mi Kyoung Park. Highly sensitive mach zehnder interferometer biosensor based on silicon nitride slot waveguide. *Sensors and Actuators B: Chemical*, 188:681–688, 2013. (Cited on page 2)

[9] Kun Qin, Shuren Hu, Scott T Retterer, Ivan I Kravchenko, and Sharon M Weiss. Slow light mach–zehnder interferometer as label-free biosensor with scalable sensitivity. *Optics letters*, 41(4):753–756, 2016. (Cited on page 2)

[10] Xudong Fan, Ian M White, Siyka I Shopova, Hongying Zhu, Jonathan D Suter, and Yuze Sun. Sensitive optical biosensors for unlabeled targets: A review. *analytica chimica acta*, 620(1):8–26, 2008. (Cited on page 2)

[11] Riccardo Zamboni. Caratterizzazione microfluidica di un generatore di gocce a t-junction integrato in niobato di litio. Master's thesis, Department of Physics in Università degli Studi di Padova, 9 2014. (Cited on pages 5, 13, 14, 16, 50 e 52)

[12] Michael Esseling, Annamaria Zaltron, Cinzia Sada, and Cornelia Denz. Charge sensor and particle trap based on z-cut lithium niobate. *Applied Physics Letters*, 103(6):061115, 2013. (Cited on page 5)

[13] Michael Esseling, Annamaria Zaltron, Nicola Argiolas, Giovanni Nava, Jörg Imbrock, Ilaria Cristiani, Cinzia Sada, and Cornelia Denz. Highly reduced iron-doped lithium niobate for optoelectronic tweezers. *Applied Physics B*, 113(2):191–197, 2013. (Cited on page 5)

[14] Michael Esseling, Annamaria Zaltron, Wolfgang Horn, and Cornelia Denz. Optofluidic droplet router. *Laser and Photonics Reviews*, 9(1):98–104, 2015. (Cited on page 5)

[15] T. Volk and M. Wöhlecke. *Lithium Niobate: defects, photorefraction and ferroelectric switching*, volume 115. Springer Science and business Media, 2008. (Cited on page 6)

[16] Rauber A. *Chemistry and physics of lithium niobate*, volume 1. Current topic in materials science, 1978. (Cited on page 6)

[17] P. Lerner, C. Legras, and J. Dumas. Stechiometrie des monocristaux de metaniobate de lithium. *Journal of crystal Growth*, 3:231–235, 1968. (Cited on page 8)

[18] W. Sohler, D. Dibyendu, and R. Selim *et al.* Erbium-doped lithium niobate waveguide lasers. *IEICE transactions on electronics*, 88(5):990–997, 2005. (Cited on page 8)

[19] M. Wöhlecke, G. Corradi, and K. Betzler1. Optical ethods to characterise the composition and homogeneity of lithium niobate single crystal. *Applied physics B*, 63(4):323–330, 1996. (Cited on page 9)

[20] M. Luennmann, U. Hartwing, and G. Panotopopulos *et al*. Electrooptic properties of lithium niobate for extremely high external electric fields. *Applied Physics B*, 76(4): 403–406, 2003. (Cited on page 10)

[21] E. Bernal, G. Chen, and T. Lee. Low frequency electro-optic and dielectric constants of lithium niobate. *Physics Letters*, 21(3):259–260, 1966. (Cited on page 10)

[22] EL. Wooten, KM. Kissa, A. Yi-Yan, and et al. A review of lithium niobate modulators for fiber-optic communications system. *Selected Topics in IEEE Jornual of Quantum Electronics*, 6(1):69–82, 2000. (Cited on pages 10, 24 e 27)

[23] XY. Du, ME. Swanwick, YQ. Fu, and et al. Surface acoustic wave induced streaming and pumping in 128°y-cut $LiNbO_3$ for microfluidic applications. *Journal of Micromechanics and Microengineering*, 19(3):35016, 2009. (Cited on page 11)

[24] R. Weis and T. Gaylord. Lithium niobate: summary of physical properties and crystal structure. *Applied Physics A*, 37(4):191–203, 1985. (Cited on page 11)

[25] S. Grilli and P. Ferraro. Dielectrophoresic trapping of suspended particles by selective pyroelectris effect in lithium niobate crystals. *Applied Physics Letters*, 92(23):232902, 2008. (Cited on page 11)

[26] S.G. et al. P.F., S.C. Dispensing nano-pico droplets and liquid patterning by pyroelectrodynamic shooting. *Nat Nano*, 5(6):429–435, 2010. (Cited on page 11)

[27] G. Whitesides and A. Stroock. Flexible methods for microfluidics. *Physics Today*, 54(6): 42, june 2001. (Cited on page 13)

[28] G. Whitesides and A. Stroock. Components for integrated poly(dimethylsiloxane) microfluidic system. *Electrophoresis*, 23(20):3461–3473, 2002. (Cited on page 13)

[29] G. Pozza, S. Kroesen, G. Bettella, A. Zaltron, M. Esseling, G. Mistura, P. Sartori, E. Chiarello, M. Pierno, C. Denz, and et al. T-junction droplet generator realised in lithium niobate crystals by laser ablation. *Optofluics, Microfluidics and Nanofluidics*, 1(1), 2014. (Cited on pages 13, 16 e 17)

[30] Giacomo Bettella. *Integrated Opto-Microfluidic Lab-on-a-Chip in Lithium Niobate for Droplet Generation and Sensing*. PhD thesis, Department of Physics in Università degli Studi di Padova, 9 2015. (Cited on pages 13, 21, 22, 23, 24, 52, 65 e 74)

[31] G. Bettella, G. Pozza, A. Zaltron, MV. Ciampolillo, N. Argiolas, C. Sada, M. Chauvet, and B. Guichardaz. Integrated opto-microfluidics platforms in lithium niobate crystals for sensing applications. In *SPIE OPTO*, pages 936517–936517. International Society for Optics and Photonics, 2015. (Cited on pages 13 e 18)

[32] GF Christopher, NN Noharuddin, and Ja *et al.* Taylor. Experimental observations of the squeezing to dripping transition in t-shaped microfluidic junctions. *Physical Review E-Statistical, Nonlinear, and Soft Matter Physics*, 78(3):1–2, 2008. (Cited on pages 14 e 15)

[33] H. Stone. On lubrication flows in geometries with zero local curvature. *Chemical Engineering Science*, 60(17):4838–4845, 2005. (Cited on page 15)

[34] Carlo Montevecchi. Integrated opto-microfluidic lab-on-a-chip in lithium niobate for sensing apllications. Master's thesis, Department of Physics in Università degli Studi di Padova, 3 2015. (Cited on pages 16, 35, 52 e 74)

[35] M. Chauvet, L. Al Fares, and F. Devaux. Self trapped beams for fabrication of optofluidic chips. *Proc. SPIE*, 2012. (Cited on page 16)

[36] M. Chauvet, L. Al Fares, B. Guichardaz, F. Devaux, and S. Ballandras. Integrated optofluidic index sensor based on a self-trapped beams in $LiNbO_3$. *Applied Physics Letters*, 110(18), 2012. (Cited on page 16)

[37] H Hu, R Ricken, W Sohler, and RB Wehrspohn. Lithium niobate ridge waveguides fabricated by wet etching. *IEEE Photonics Technology Letters*, 19(6):417–419, 2007. (Cited on pages 17 e 25)

[38] M. Tamura and S. Yoshikado. Etching characteristics of $LiNbO_3$ crystal by fluorine gas plasma reactive ion etching. *Science and Technology of Advanced Materials*, 2(3-4), 2001. (Cited on page 17)

[39] z. Ren, P. J. Heard, J. M. Marshall, P. A. Thomas, and S. Yu. Etching characteristics of $LiNbO_3$ inn reactive ion etching and inductively coupled plasma. *Journal of Applied Physics*, 103(3), 2008. (Cited on page 17)

[40] F. A. Stevie, L. A. Giannuzzi, B. I. Prenitzer (auth.), Lucille A. Giannuzzi, and Fred A. Stevie (eds.). *Introduction to Focused Ion Beams: Instrumentation, Theory, Techniques and Practice*. Springer US, 1 edition, 2005. (Cited on page 17)

[41] G. Della Valle, R. Osellame, and P. Laporta. Micromachining of photonic devices by femtosecond laser pulses. *Journal of Optics A: Pure and Applied Optics*, 11(1):013001, 2009. (Cited on page 17)

[42] R. R. Gattass and E. Mazur. Femtosecond laser micromachining in transparent materials. *Nature photonics*, 2(4):219–225, 2008. (Cited on page 17)

[43] Z. Y. A. Al-Shibaany, J. Hedley, D. Huo, and Z. Hu. Micromachining lithium niobate for rapid prototyping of resonant biosensors. In *IOP Conference Series: Materials Science and Engineering*, volume 65, page 012030. IOP Publishing, 2014. (Cited on page 18)

[44] T. Young. An essay on the cohesion of fluids. *Philosophical Transactions of the Royal Society of London*, pages 65–78, 1805. (Cited on page 21)

[45] K. Sugii, M. Fukuma, and H. Iwasaki. A study on titanium diffusion into $LiNbO_3$ waveguides by electron probe analysis and x-ray diffraction methods. *Journal of Materials Science*, 13(3):523–533, 1978. (Cited on page 24)

[46] GJ. Griffiths and RJ. Esdaile. Analysis of titanium diffused planar optical waveguides in lithium niobate. *IEEE Journal of Quantum Electronics*, 20(2):149–159, 1984. (Cited on page 24)

[47] Korkishko YN and Fedorov VA. *Ion exchange in single crystals for integrated optics and optoelectronics*. Cambridge Int Science Publishing, 1999. (Cited on page 24)

[48] F. Chen, Xl. Wang, and KM. Wang. Development of ion-implanted optical waveguides in optical materials: A review. *Optical materials*, 29(11):1523–1542, 2007. (Cited on page 24)

[49] O. Peña-Rodriguez, J. Olivares, M. Carrascosa, and et al. *Optical waveguides fabricated by ion implantation/irradiation: A review*. Ion implantation, Prof. Mark Goorsky (Ed.), ISBN, 2012. (Cited on page 24)

[50] G. Bentini, M. Bianconi, L. Correra, and et al. Damage effects produced in the near surface region of x-cut $LiNbO_3$ by low dose, high energy implantation of nitroge, oxygen, adn fluorine ions. *Journal of Applied Physics*, 96(1):242–247, 2004. (Cited on page 24)

[51] JJ. Yin, F. Lu, XB. Ming, and et al. Theoretical modeling of refractive index in ion implanted $LiNbO_3$ waveguides. *Journal of Applied Physics*, 108(3):033105, 2010. (Cited on page 24)

[52] K. Itoh, O. Matobe, and Y. Ichioka. Fabrication experiment of photorefractive three-dimensional waveguides in lithium niobate. *Optics Letters*, 19(9):652–654, 1994. (Cited on page 25)

[53] J. Burghoff, C. Grebing, S. Nolte, and et al. Waveguides in lithium niobate fabricated by focused ultrashort laser pulses. *Applied surface science*, 253(19):7899–7902, 2007. (Cited on page 25)

[54] Ulliac G. Courjal N., Guichardaz B. and et al. High aspect ratio lithium niobate ridge waveguides fabricated by optical grade dicing. *Journal of Physics D: Applied Physics*, 44 (30):305101, 2011. (Cited on page 25)

[55] Matano C. On the relation between the diffusion-coefficients and concentrations of solid metals(nickel-copper system). *Japanese Journal of Physics*, 8(3), 1933. (Cited on page 26)

[56] Bahaa EA Saleh, Malvin Carl Teich, and Bahaa E Saleh. *Fundamentals of photonics*, volume 22. Wiley New York, 1991. (Cited on page 28)

[57] Iain Anderson. Transmission performance of y-junctions in planar dielectric waveguide. *IEE Journal of Microwaves Optics and Acoustics*, 2:7–12, 1978. (Cited on page 29)

[58] WK Burns, RP Moeller, CH Bulmer, and H Yajima. Optical waveguide channel branches in ti-diffused linbo 3. *Applied optics*, 19(17):2890–2896, 1980. (Cited on page 29)

[59] Masayuki Izutsu, Yoshiharu Nakai, and Tadasi Sueta. Operation mechanism of the single-mode optical-waveguide y junction. *Optics letters*, 7(3):136–138, 1982. (Cited on page 29)

[60] Masamitsu Masuda and Gar Lam Yip. An optical te-tm mode splitter using a linbo3 branching waveguide. *Applied Physics Letters*, 37(1):20–22, 1980. (Cited on page 29)

[61] K. Burns William and A. Fenner Milton. Mode conversion in planar-dielectric separating waveguides. *IEEE Journal of Quantum Electronics*, QE-11(1), January 1975. (Cited on page 29)

[62] William K Burns and A Fenner Milton. An analytic solution for mode coupling in optical waveguide branches. *IEEE Journal of Quantum Electronics*, 16:446–454, 1980. (Cited on page 30)

[63] R. Baets and P. E. Lagasse. Calculation of radiation loss in integrated-optic tapers and y-junctions. *Applied Optics*, 21(11), June 1982. (Cited on pages 31, 32 e 33)

[64] H. Kogelnik. *Topics in Applied Physics*, volume 7. Springer, 1979. (Cited on page 31)

[65] R. Baets and P. E. Lagasse. Loss calculation and design of arbitrarily curved integrated-optic waveguides. *American Optical Society*, 73(2), February 1983. (Cited on pages 34 e 35)

[66] H Sasaki and N Mikoshiba. Normalised power transmission in single mode optical branching waveguides. *Electronics Letters*, 17:136–138, 1981. (Cited on pages 42 e 43)

[67] G. Binnig, C. F. Quate, and Ch. Gerber. Atomic force microscope. *Phys. Rev. Lett.*, 56: 930–933, Mar 1986. (Cited on page 42)

[68] Miyazawa H. Nozawa T. and Miyazawa S. Water vapor effects on titanium diffusion into $LiNbO_3$ substrates. *Japanese Journal of Applied Physics*, 29(10R), 1990. (Cited on page 44)

[69] Makoto Minakata, Shoichi Saito, Masashi Shibata, and Shintaro Miyazawa. Precise determination of refractive-index changes in ti-diffused linbo3 optical waveguides. *Journal of Applied Physics*, 49(9):4677–4682, 1978. (Cited on page 47)

[70] F Caccavale, P Chakraborty, A Quaranta, I Mansour, G Gianello, S Bosso, R Corsini, and G Mussi. Secondary-ion-mass spectrometry and near-field studies of ti:linbo3 optical waveguides. *Journal of applied physics*, 78(9):5345–5350, 1995. (Cited on page 47)

[71] Fernanda Irrera and Marco Valli. Characterization of planar $TiLiNbO_3$ optical waveguides in the visible and near infrared spectral range. *Journal of Applied Physics*, 64(4), 1988. (Cited on page 56)

[72] M. Armenise, C. Canali, M. De Sario, and et al. Evaluation of the ti diffusion process during fabrication of ti: $LiNbO_3$ optical waveguides. *Journal of Non-Crystalline Solids*, 47 (2):255–257, 1982.